JM PAPERS

Fully nonlinear simulations of rogue wave formation in finite-depth irregular waves

Yanyan Zhai[1] ⓘ, Mathias Klahn[2] ⓘ, Miguel Onorato[3] ⓘ and David R. Fuhrman[1] ⓘ

[1]Department of Civil and Mechanical Engineering, Technical University of Denmark, 2800 Kgs. Lyngby, Denmark

[2]Niels Bohr Institute, University of Copenhagen, 2200 Copenhagen N, Denmark

[3]Dipartimento di Fisica Generale, Università di Torino, Via P Giuria 1 Torino, Italy

Corresponding author: David R. Fuhrman, drfu@dtu.dk

Numerical studies on the statistical properties of irregular waves in finite depth have to date been based on models founded on weak nonlinearity; as a consequence, only lower-order (usually third-order) nonlinear interactions have thus far been investigated. The present study performs numerical simulations with a fully nonlinear, spectrally accurate model to investigate the statistics of irregular, unidirectional wave fields in finite water depth initially given by a Texel, Marsen and Arsloe spectrum. A series of random unidirectional wave fields are considered, covering a wide range of water depth. The wave spectrum and statistical properties, including the probability density function of the surface elevation, exceedance probability of wave crests and occurrence probability of extreme (rogue) waves, are investigated. The importance of full nonlinearity in comparison with third-order results is likewise evaluated. The results show that full nonlinearity increases kurtosis and enhances the occurrence probability of large wave crests and rogue waves substantially, in both deep water and finite water depth. Therefore, we propose that full nonlinearity may contribute significantly to the formation of rogue waves. Furthermore, to account for the effects of higher-order nonlinearity on modulational instability, we analyse the relationship between the Benjamin–Feir index (BFI) and maximal excess kurtosis. Our results show a strong linear relationship i.e. $(\mathcal{K}_{max} - 3) \propto \mathrm{BFI}$, in contrast to $(\mathcal{K}_{max} - 3) \propto \mathrm{BFI}^2$ based on the assumptions of weak nonlinearity, a narrow-banded spectrum and deep-water conditions. Above, $\mathcal{K}_{max}$ is the maximal kurtosis.

Key words: coastal engineering, nonlinear instability, surface gravity waves

1. Introduction

Rogue waves, the extreme wave events occurring within irregular waves, have been reported worldwide from ships, offshore platforms and radars (e.g. Kharif & Pelinovsky 2003; Forristall 2005). Due to anticipated increased storminess in e.g. Northern Europe as a consequence of climate change, such extreme waves are expected to be increasingly common in the future. Rogue waves have, on multiple occasions, proven lethal to ships, offshore structures and their operators (e.g. Kharif & Pelinovsky 2003; Dysthe, Krogstad & Müller 2008; Kharif, Pelinovsky & Slunyaev 2008; Slunyaev, Didenkulova & Pelinovsky 2011), with some of the most extreme events ever documented occurring in conditions of finite depth with $kh < 2$, k being the characteristic wavenumber and h the water depth (e.g. Hayer & Andersen 2000; Chien, Kao & Chuang 2002; Trulsen 2007; Babanin *et al.* 2011). Accurate evaluation regarding the statistical properties of random wave fields and understanding the mechanisms generating rogue waves are essential towards ensuring the safety of shipping, as well as proper design (both preventing failure and excessive over-design) of offshore wind turbines and other structures.

The occurrence of rogue waves has been attributed to a variety of physical mechanisms (e.g. Kharif & Pelinovsky 2003; Onorato *et al.* 2013; Adcock & Taylor 2014). In addition to the linear superposition of dispersive waves and linear mechanisms linked to wave refraction (e.g. Lavrenov 1998; White & Fornberg 1998), nonlinear modulational instability (MI, or Benjamin–Feir instability, also known as the class-I instability) is often cited as a potential generation mechanism (e.g. Henderson, Peregrine & Dold 1999; Tulin & Waseda 1999). The MI occurring in narrow-band irregular wave fields is suppressed by decreased water depth. Benjamin & Feir (1967) and Whitham (1974) first showed that the one-dimensional (1-D) (i.e. a single horizontal direction) MI disappears for dimensionless water depths $kh < 1.363$. Including directional (non-collinear) disturbances, the critical water depth decreases, meaning that the class-I MI can still exist for $kh < 1.363$, as was shown by Davey & Stewartson (1974) and McLean (1982*a*).

In the past decades, the relationship of MI to rogue wave formation has been widely studied through theoretical, experimental and numerical methods. In unidirectional wave fields, Janssen (2003) theoretically proposed the Benjamin–Feir index (BFI), corresponding to the ratio of wave steepness to spectral bandwidth, to quantify the importance of MI. In other words, the larger the BFI, the more significant the MI. In special situations where the wave field is represented by a narrow-band spectrum, this theory is restricted to the consideration of up to four-wave interactions. Under these conditions, the long-term excess kurtosis has been found to be proportional to BFI^2 (e.g. Mori & Yasuda 2002; Mori & Janssen 2006). As the kurtosis increases, the probability of rogue waves increases (e.g. Xiao *et al.* 2013; Liu *et al.* 2022). In addition, a series of laboratory experiments also support this relationship between kurtosis and rogue wave occurrence (e.g. Onorato *et al.* 2004; Shemer & Sergeeva 2009; Shemer, Sergeeva & Slunyaev 2010).

Apart from theoretical analysis and experiments, existing numerical investigations have mostly employed the so-called high-order spectral (HOS) method of West *et al.* (1987) and Dommermuth & Yue (1987) (e.g. Toffoli *et al.* 2010; Xiao *et al.* 2013; Fernandez *et al.* 2014; Liu *et al.* 2022) truncated at low (typically third) order, models based on the Zakharov equation (e.g. Janssen & Onorato 2007; Annenkov & Shrira 2009) or its narrow-band limit the nonlinear Schrödinger equation (e.g. Onorato *et al.* 2001; Gramstad & Trulsen 2011; Dong *et al.* 2018). These methods are all effectively weakly nonlinear, and they can only be used to study low-order nonlinear wave–wave interactions. Furthermore, some fully nonlinear simulations for unidirectional waves have been carried out, such as Zakharov, Dyachenko & Vasilyev (2002), Chalikov (2009) and Slunyaev & Sergeeva (2012). These simulations revealed that high-order nonlinearities

have the potential to alter the statistical properties of deep-water waves. Notably, a strong correlation between kurtosis and rogue wave formation was identified. Nonetheless, it is important to acknowledge that these investigations are thus far constrained to the context of deep-water conditions. As far as the authors are aware, in finite water depth, the impact of full nonlinearity on both MI and random wave statistical properties has not yet been explored. Consequently, there remains a gap in the understanding of the relationship between full nonlinearity (greater than third order in the context of HOS simulations) and the probability of rogue wave occurrence.

In the present paper, we perform a series of numerical simulations with the fully nonlinear pseudospectral Fourier–Legendre (PFL) potential flow model of Klahn, Madsen & Fuhrman (2021*d*) for unidirectional irregular wave fields in finite depth. This model is chosen due to its thorough examination in the previous studies of Klahn *et al.* (2021*c*,*b*), which demonstrated its capability to precisely and efficiently simulate highly nonlinear wave–wave interactions without resorting to any weakly nonlinear approximations. This paper will partially fill the voids associated with fully nonlinear wave–wave interactions in a single horizontal direction in finite depth, as described above, by analysing the statistical properties of irregular waves, such as the probability density function (PDF) of surface elevation and wave crest distribution, and the probability of rogue wave occurrence. The resulting statistical properties will be analysed and compared with third-order simulations utilising the HOS method (e.g. Liu *et al.* 2022). It will be shown that, compared with third-order HOS results, full nonlinearity gives rise to a greater exceedance probability of both wave crests and kurtosis. The PDF of the surface elevation will also be shown to deviate significantly from second-order theoretical and third-order HOS simulation results with respect to the negative and positive tails when $kh > 1.363$. It will also be clarified that full nonlinearity can result in larger occurrence probability of rogue waves based on these statistical properties.

The remainder of the present paper is organised as follows: in § 2, we describe the governing equations and numerical methods used for time integration of wave fields. We then proceed to validate the numerical model for cases involving pure 1-D MI in deep-water conditions in § 3. This validation specifically focuses on assessing the initial exponential growth rate of the unstable sidebands, in addition to the phenomena of recurrence (at low initial steepness) and frequency downshift (at larger initial steepness). The fully nonlinear simulations of unidirectional irregular waves in finite depth will be presented in § 4, including description of the initial conditions utilised, and subsequent discussion of obtained results. Based on the statistical results, the dependence of kurtosis on BFI is analysed and compared in § 5. Conclusions are finally drawn in § 6.

2. Model description

Following Klahn *et al.* (2021*d*), we consider the time evolution of 2-D irregular wave fields in both deep and finite water, assuming they satisfy the conditions of potential flow and have a non-overturning free surface. Additionally, we take the wave fields to be periodic in the x-direction over distance L_x. Once the initial conditions for the wave fields have been specified, their time evolution is completely determined by the irrotational Euler equations. As has, for example, been shown by Zakharov (1968), this system of equations may be written as

$$\frac{\partial^2 \Phi}{\partial x^2} + \frac{\partial^2 \Phi}{\partial z^2} = 0 \ \ \text{if} \ z < \eta, \tag{2.1a}$$

$$\frac{\partial \Phi}{\partial z}\bigg|_{z=-h} = 0, \tag{2.1b}$$

$$\frac{\partial \eta}{\partial t} = \left(1 + \left(\frac{\partial \eta}{\partial x}\right)^2\right) v_z^{(s)} - \frac{\partial \eta}{\partial x}\frac{\partial \Phi_s}{\partial x}, \tag{2.1c}$$

$$\frac{\partial \Phi_s}{\partial t} = -g\eta - \frac{1}{2}\left(\frac{\partial \Phi_s}{\partial x}\right)^2 + \frac{1}{2}\left(1 + \left(\frac{\partial \eta}{\partial x}\right)^2\right)\left(v_z^{(s)}\right)^2, \tag{2.1d}$$

where η denotes the free surface elevation, $\Phi_s \equiv \Phi|_{z=\eta}$ is the velocity potential at the surface, $v_z^{(s)} \equiv \partial_z \Phi|_{z=\eta}$ is the vertical velocity of the fluid at the free surface and g is the gravitational acceleration. This set of equations constitutes an initial value problem for the pair (η, Φ_s), and so the initialisation of the system amounts to initialising these two variables.

The PFL potential flow simulation model of Klahn *et al.* (2021*d*) adopted in the present study is spectrally accurate in all spatial directions, by which we mean that all spatial dependencies are approximated through generalised Fourier series, which, for this particular problem, guarantees that the error of the numerical solution decays exponentially with the resolution. All details of the numerical scheme are explained in Klahn *et al.* (2021*d*). This method adopts a positive number b to make use of an artificial lower (i.e. beneath trough) boundary condition based on Nicholls (2011), with iterative solutions to the resulting Laplace equation utilising a linearised preconditioner, following the strategy of Fuhrman & Bingham (2004). Furthermore, this model utilises the Fourier collocation method and the classical fourth-order Runge–Kutta method to discretise the spatial and temporal parts of the free surface boundary conditions, respectively. To avoid instabilities during simulations, which may arise due to both nonlinearity as well as the inability to simulate breaking, the artificial damping strategy outlined by Xiao (2013) is employed, as described in Klahn *et al.* (2021*d*). For full details on this model, features, and prior validations and applications see Klahn *et al.* (2021*b*,*c*,*d*, 2024) in addition to Fuhrman, Klahn & Zhai (2023).

3. Sideband instability of modulated wave trains

In this section, our focus is on investigating the classical MI of deep-water waves, which has not been considered previously with this model. Through combined theoretical and experimental work, Benjamin & Feir (1967) demonstrated that weakly nonlinear deep-water waves can experience instability in the presence of modulational perturbations when certain resonance conditions are met, which can result in the exponential growth of sideband modes. The Benjamin–Feir instability can be characterised as quartet resonant interactions involving a carrier wave and two initially small-amplitude sideband waves, subject to the following resonant conditions:

$$k_1 + k_2 = 2k_0, \quad \omega_1 + \omega_2 = 2\omega_0. \tag{3.1}$$

Here, the carrier wave is defined by its wavenumber k_0 and angular frequency ω_0, while the two (assumed initially small) perturbations are characterised by the wavenumbers $k_1 = (1 + p)k_0$, $k_2 = (1 - p)k_0$ and angular frequencies $\omega_1 = \omega_0(1 + \delta)$, $\omega_2 = \omega_0(1 - \delta)$, where $k_0 = \omega_0^2/g$ and δ is small to ensure minimal de-tuning of the resonance. As evident from the frequency expressions, the perturbation waves correspond to the unstable upper/lower sidebands of the primary wave. In the following simulations, the carrier waves are prescribed as initial conditions, based on the plane progressive streamfunction solution

of Fenton (1988). The selection of perturbation frequencies and wavenumbers is carefully made following the approach outlined by McLean (1982*b*) in deep water. Consequently, in order to induce the desired instability, two perturbations are introduced to the base variables in the x direction for both the initial free surface elevation η

$$\widetilde{\eta} = \epsilon a_0 \sin(k_j x), \tag{3.2}$$

and the velocity potential at the free surface Φ_s

$$\widetilde{\Phi}_s = \epsilon a_0 \sqrt{\frac{g}{k_j h}} \frac{\cosh(k_j(\eta + h))}{\cosh(k_j h)} \cos(k_j x), \tag{3.3}$$

where $j = 1, 2$ and a_0 is the amplitude of the carrier wave. The normalised perturbation amplitude, denoted as ϵ, represents the initial perturbation amplitudes relative to that of the carrier wave a_0.

Tulin & Waseda (1999) and Madsen, Bingham & Liu (2002) conducted numerical and experimental investigations, respectively, to explore the MI of deep-water wave trains. In their numerical study, Madsen *et al.* (2002) observed a recurrence phenomenon when wave breaking was absent. In both experiments and simulations utilising conditions where wave breaking occurred, a permanent frequency downshift was noted. In the subsequent §§ 3.1 and 3.2, we utilise the fully nonlinear potential flow model to reproduce the two specific cases considered by Tulin & Waseda (1999) and Madsen *et al.* (2002), respectively. To extend these studies and further assess the model's capability in capturing the strongly nonlinear wave dynamics under finite-depth conditions, we introduce two additional numerical experiments, presented alongside the deep-water cases in §§ 3.1 and 3.2.

3.1. *Simulations involving recurrence*

For our initial test case, we draw inspiration from the previous simulation of Madsen *et al.* (2002). Following their set-up, we utilise an initial carrier wave steepness $k_0 a_0 = 0.1$, with dimensionless depth $k_0 h = 2\pi$ (i.e. deep water). The perturbations are prescribed with $p = 0.2$ (corresponding to $\delta = k_0 a_0$) and relative steepness $\epsilon = 0.05$. The initial waves are determined and specified using the streamfunction solution of Fenton (1988). The computational domain has length $10\lambda_0$, where $\lambda_0 = 2\pi/k_0$ is the carrier wavelength, utilising periodic lateral boundary conditions. Simulations utilise 320 horizontal grid points such that the carrier wave field is resolved by $\lambda_0/\Delta x = 32$ points per wavelength, coupled with eight points distributed in the vertical direction. The time step is set such that $T_0/\Delta t = 50$, where $T_0 = 2\pi/\omega_0$ is the carrier wave period. The simulation is carried out over a duration of $500T_0$.

The primary objective of these simulations is to verify the present fully nonlinear model against the theoretical predictions of McLean (1982*b*). Specifically, we focus on assessing the initial growth rate of sidebands as a means of validation. To facilitate a spatial domain comparison, we adopt the method outlined by Benjamin & Feir (1967) and convert our simulated results from the time domain to the spatial domain using the following transformation:

$$\frac{x}{\lambda_0} = \frac{c_g t}{c_0 T_0} = \frac{1}{2} \left(1 + \frac{2k_0 h}{\sinh(2k_0 h)} \right) \frac{t}{T_0}, \tag{3.4}$$

where t is the time, c_g represents the group velocity of the primary wave train and $c_0 = \omega_0/k_0$, the celerity of the carrier wave.
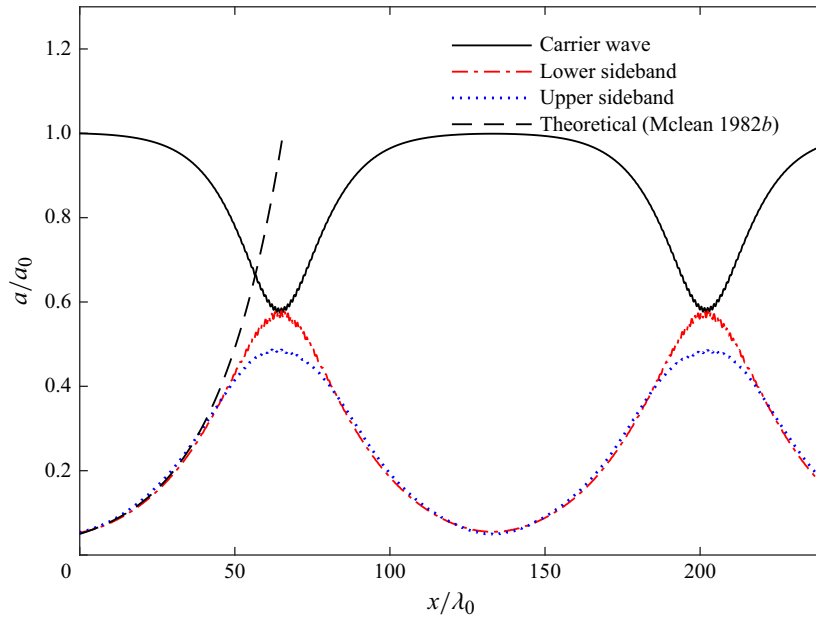
Figure 1. Computed spatial evolution of the carrier wave and sideband amplitudes from the simulated Benjamin–Feir instability for $k_0 h = 2\pi$ with low initial steepness $k_0 a_0 = 0.1$. The theoretical sideband growth rate corresponds to the evolution predicted by McLean (1982*b*).

During the initial growth stage, the theoretical sideband amplitudes will follow (McLean 1982*a*)

$$\frac{a}{a_0} = \epsilon \exp(\text{Im}\{\beta\}\sqrt{gk_0}x/c_g), \tag{3.5}$$

where $\text{Im}\{\cdot\}$ represents the imaginary part and β is the unstable eigenvalue, representing a dimensionless complex frequency in a frame of reference moving with the primary wave, stemming from the analysis of McLean (1982*a,b*). For the present case McLean's (1982*a*) analysis, as implemented in Fuhrman, Madsen & Bingham (2004), yields the dimensionless complex frequency $\beta = -0.0977 + 0.00364i$, where i is the imaginary unit. Figure 1 displays the spatial evolution of the carrier and sideband amplitudes from the present case. It is evident that the initial growth rate of the sidebands is in good agreement with that predicted by McLean's theoretical analysis. This serves as validation, particularly for the initial stage of the simulation. Following the initial stage, the exponential growth slows, with the lower sideband amplitude slightly exceeding that of the upper sideband, as also found e.g. by Lo & Mei (1985). Following their respective peaks, the simulation results in a nearly symmetric recurrence cycle, where energy is passed from the sidebands back to the carrier wave, eventually resulting in a situation resembling the initial condition, and the phenomenon repeats. The length of each cycle, defined as the distance between two minima of the carrier wave, measures approximately $138\lambda_0$. This finding agrees well with the results of Landrini *et al.* (1998) and Madsen *et al.* (2002), who reported $140\lambda_0$ and $141\lambda_0$, respectively. With this simulation, we conclude that the present fully nonlinear model is capable of simulating the Benjamin–Feir instability with low initial carrier wave steepness.

Following the deep-water case, we next consider a simulation in finite water depth with $k_0 h = 2$, again starting with an initial carrier wave steepness of $k_0 a_0 = 0.1$.
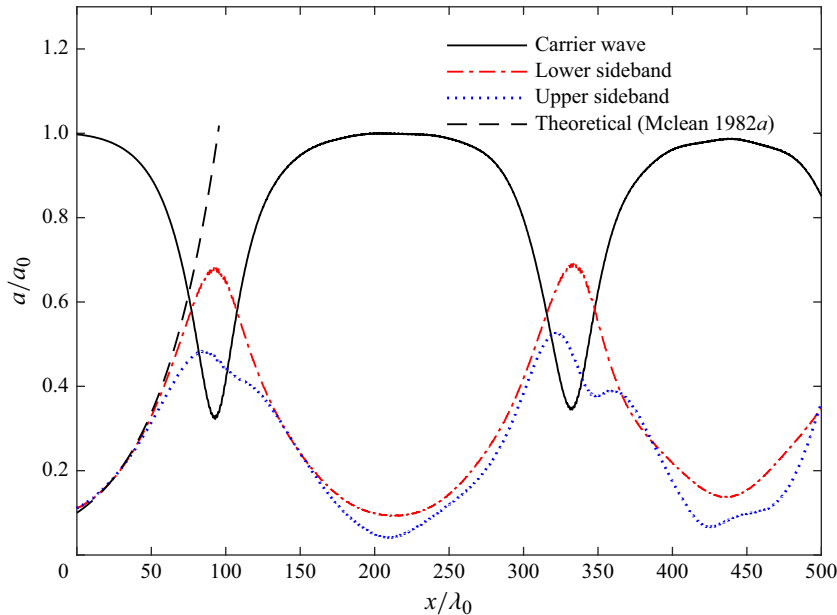
Figure 2. Computed spatial evolution of the carrier wave and sideband amplitudes from the simulated Benjamin–Feir instability for $k_0 h = 2$ with moderate initial steepness $k_0 a_0 = 0.1$. The theoretical sideband growth rate corresponds to the evolution predicted by McLean (1982a).

The perturbations are prescribed with $p = 0.1$ and $\epsilon = 0.1$. The total simulation duration is extended to $900 T_0$, while all other computational parameters are identical to those used in the deep-water case. The dimensionless complex frequency associated with this case is $\beta = -0.0410 + 0.00218i$. Figure 2 presents the computed spatial evolution of the carrier wave and sideband amplitudes for this finite-depth case, considering the transformation described by (3.4). As shown, the sideband amplitudes initially exhibit exponential growth, closely matching the theoretical prediction of McLean (1982a), which can be taken as model validation. After reaching their peak values, a recurrence phenomenon develops, characterised by the transfer of energy from the sidebands back to the carrier wave, similar to the behaviour observed in the deep-water recurrence case. These results further demonstrate the capability of the present fully nonlinear model to accurately simulate the Benjamin–Feir instability under varying depth conditions.

3.2. *Simulations involving frequency downshift*

As demonstrated in the preceding case, a local frequency downshift occurs when the sideband amplitudes are near their respective peaks. Nevertheless, it is crucial to acknowledge that this downshift is temporary in nature, as the modulational process is cyclical. On the contrary, experiments conducted by Tulin & Waseda (1999), leading to wave breaking, have revealed a permanent downshift of the peak frequency. Simultaneously, the amplitudes of both the carrier wave and upper sideband decrease, while the lower sideband experiences a permanent increase in amplitude. In the following, we will examine one of their cases involving a brief wave breaking around the first modulational peak. The water depth is set as $h = 1.2$ m, consistent with the value employed in previous studies such as Madsen *et al.* (2002) and Li & Fuhrman (2022), rather than the 2.1 m utilised in the experimental set-up. A carrier wave characterised by $\lambda_0 = 1.2$ m (corresponding to $\omega_0 = 1.14$ s^{-1} and $k_0 h = 2\pi$ i.e. deep water) and $k_0 a_0 = 0.133$ is
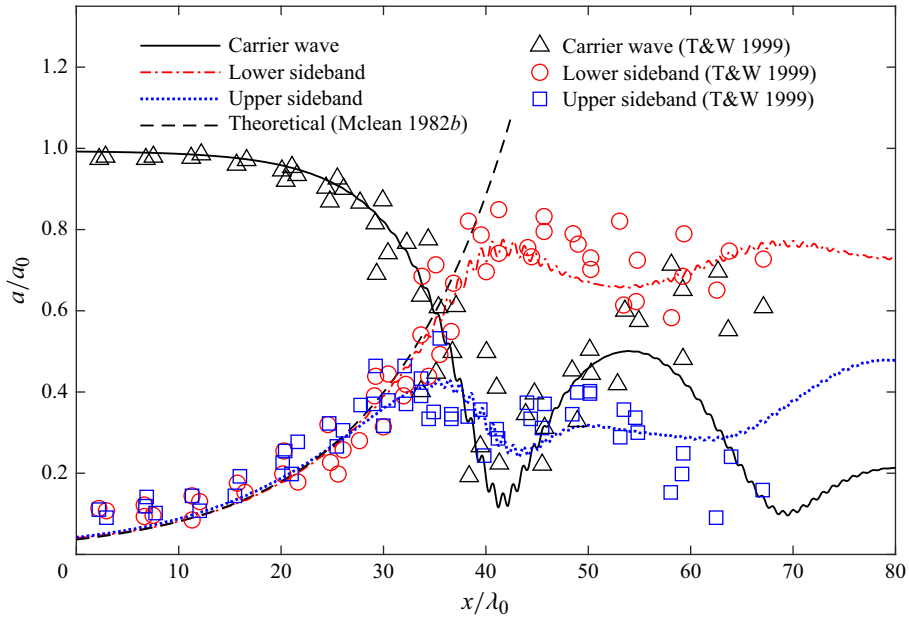
Figure 3. Computed spatial evolution of the carrier wave and sideband amplitudes from the simulated Benjamin–Feir instability with larger initial steepness $k_0 a_0 = 0.133$. The theoretical sideband growth rate corresponding to the evolution predicted by McLean (1982*b*), and T&W 1999 represents the experimental data of Tulin & Waseda (1999).

used. Notably, the chosen steepness $k_0 a_0$ exceeds the breaking threshold value of 0.1125 according to Banner & Tian (1998) and Henderson *et al.* (1999). Consequently, the occurrence of dissipative breaking would be anticipated from a physical perspective. The perturbations are generated using parameters $\delta = 0.785 k_0 a_0$, which corresponds to $p = 0.2$, from which the stability analysis of McLean (1982*a*) yields the unstable eigenvalue $\beta = -0.0963 + 0.00639i$, the perturbation strength is set to $\epsilon = 0.03$. The total simulation time is $200 T_0$. The remaining computed parameters, such as the domain size and resolution, remain consistent with those utilised in § 3.1.

The present fully nonlinear simulation is quantitatively validated in figure 3, again making use of (3.4). Here the spatial evolution of amplitudes (carrier wave plus both sidebands) is compared with the experimental data from Tulin & Waseda (1999). We likewise verify the initial exponential growth rate of the sidebands against the theoretical prediction of McLean (1982*a*), based on the unstable eigenvalue reported above. Figure 3 demonstrates a good match of the initial sideband growth rate with the theoretical prediction. This match is maintained longer for the lower sideband than the upper. Furthermore, the initial and longer term evolutions of both the carrier wave and the sidebands exhibit reasonable agreement with the experimental data of Tulin & Waseda (1999). Around the vicinity of the first modulational peak, approximately at $x \approx 42 \lambda_0$, the primary wave undergoes a decrease, reaching a local minimum before gradually rising again. However, it does not fully regain its original strength attained prior to wave breaking. This phenomenon has also been confirmed through other experimental studies (Melville 1982). It is also observed that the lower sideband consistently maintains the highest amplitude (around $0.75 a_0$), while both the carrier wave and upper sideband experience fluctuations at much lower levels. Consequently, this confirms the occurrence of a permanent frequency downshift for larger initial carrier wave
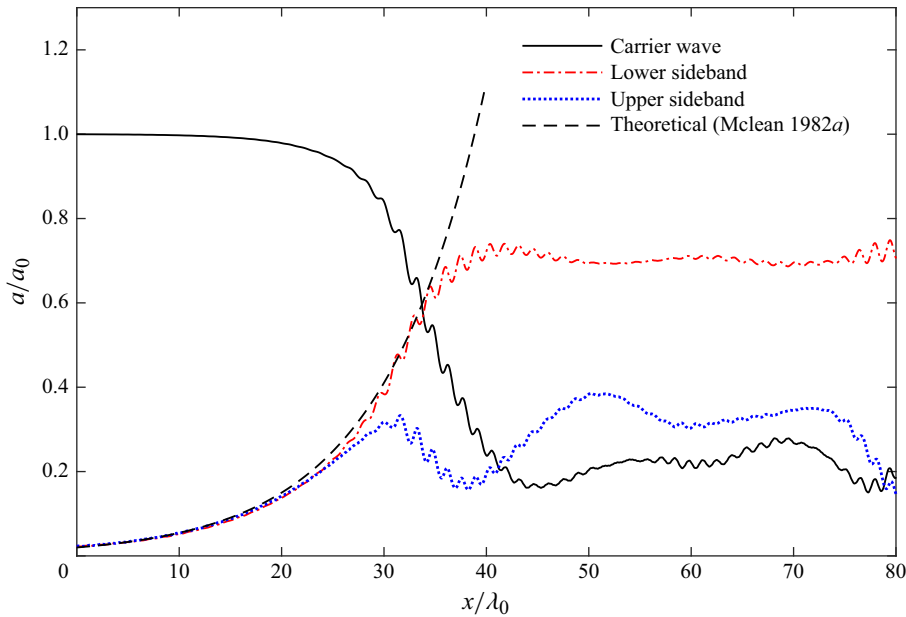
Figure 4. Computed spatial evolution of the carrier wave and sideband amplitudes from the simulated Benjamin–Feir instability for $k_0 h = 2$ with initial steepness $k_0 a_0 = 0.2$. The theoretical sideband growth rate corresponding to the evolution predicted by McLean ([1982a](#)).

steepness. Physically, this phenomenon is related to dissipative wave breaking around the modulation peak. The present simulated results are likewise in close agreement with those reported previously, either utilising potential flow models (Madsen *et al.* 2002) or more advanced computational fluid dynamics models (Li & Fuhrman 2022) which directly simulated the wave breaking process.

Further validation of the present model's ability to simulate strongly nonlinear wave evolution at finite depth is achieved through an additional numerical experiment with parameters $p = 0.2$, $k_0 a_0 = 0.2$ and $\epsilon = 0.02$, while maintaining all other computational parameters identical to the deep-water frequency downshifted case. The unstable eigenvalue $\beta = -0.0764 + 0.00902i$, obtained from the finite-depth stability analysis of McLean (1982a), is employed to verify the initial sideband growth rate. As shown in figure 4, the simulated sideband amplitudes initially exhibit exponential growth, closely matching the theoretical prediction up to approximately $x \approx 35\lambda_0$ for the lower sideband. Beyond the first modulational peak, a permanent frequency downshift is established, characterised by a sustained reduction in the carrier wave amplitude, associated with dissipative effects linked to wave breaking, and consistent with behaviour observed under deep-water conditions. These results further validate the present model's accuracy in capturing steep wave evolution under finite-depth conditions.

3.3. *Modelling energy dissipation*

For the long-time simulations considered herein, it is essential to account for potential energy dissipation during wave evolution. To quantify the energy loss, the total mechanical energy is computed following the formulation of Klahn *et al.* (2021a,b) as

$$E = \frac{1}{2} \int_0^{L_x} \left(\Phi_s \frac{\partial \eta}{\partial t} + g\eta^2 \right) \mathrm{d}x, \tag{3.6}$$
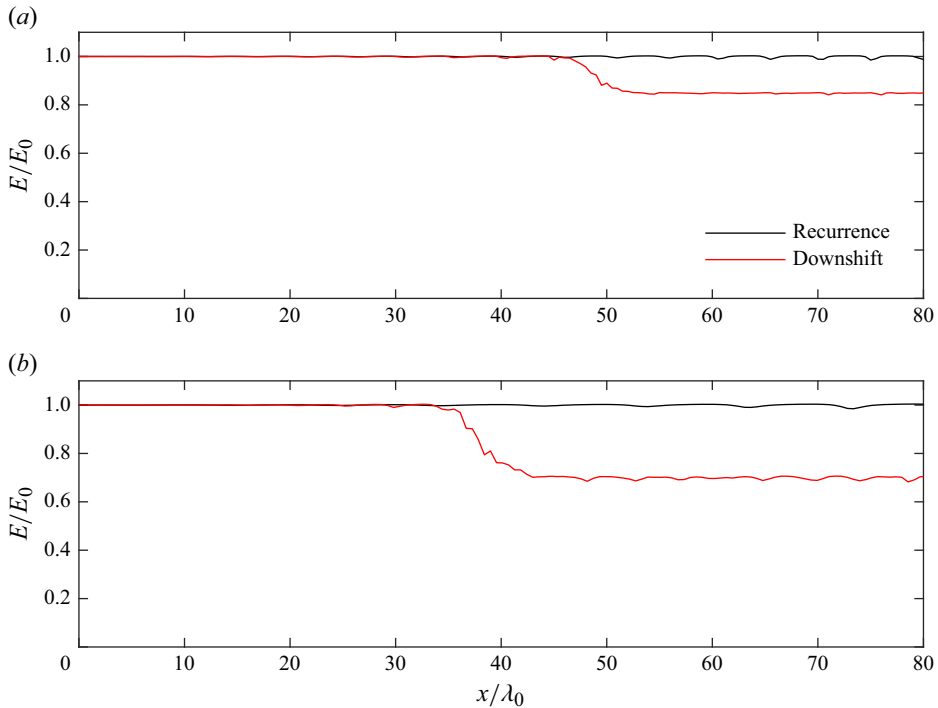
Figure 5. Spatial evolution of the total mechanical energy for wave fields exhibiting recurrence and frequency downshift, shown for $k_0 h = 2\pi$ (*a*) and $k_0 h = 2$ (*b*).

where L_x denotes the horizontal extent of the computational domain. The spatial evolution of the total energy for the simulations, using (3.4) and discussed in §§ 3.1 and 3.2, is presented in figure 5. Notably, there is no sign of energy loss in the simulations involving recurrence. In contrast, simulations exhibiting frequency downshift preserve $E/E_0 \approx 1$ during the initial stage, followed by a rapid decline of approximately 15 % and 31 % over a spatial interval of roughly $10\lambda_0$, for $k_0 h = 2\pi$ and $k_0 h = 2$, respectively. In deeper water (figure 5*a*), stronger dispersion delays sideband saturation and thus limits energy loss, whereas in finite depth (figure 5*b*), reduced dispersion accelerates sideband growth and precipitates larger, earlier energy dissipation. Comparison with figures 3 and 4 confirms that irreversible energy dissipation contributes to the establishment of a permanent frequency downshift.

4. Simulations of irregular waves

Having validated the model for cases involving MI of regular wave trains in the previous section, the present section will present numerical simulations examining the impact of full (beyond third-order) nonlinearity in the simulation of realistic frequency spectra. Within this framework, a series of unidirectional irregular wave simulations are conducted in both deep and finite depths using the fully nonlinear model. This work is inspired by the study of Liu *et al.* (2022). They carried out unidirectional irregular wave simulations using HOS method truncated at third order to study the relationship between rogue wave formation and BFI. The initial conditions and parameters used in our simulations will be described in § 4.1. In § 4.2 we consider some specific properties of the wave field such as the energy wave spectrum and significant wave height at different peak periods. Furthermore, we also consider some specific statistical properties of the surface elevation and contrast them

with third-order HOS results of Liu *et al.* (2022). In §4.3 we investigate the skewness and kurtosis of the surface elevation as well as its PDF, and in that connection we will work with spatial averages. In §4.4 we consider the exceedance probability of the wave crest and probability of rogue wave occurrence.

4.1. *Initial conditions and computational parameters*

In the forthcoming simulations with the present model, the initial conditions for (η, Φ_s) are constructed by linearly combining sinusoidal wave components with random phases uniformly distributed in the range of $[0, 2\pi]$. Each component is characterised by its angular frequency ω and amplitude chosen based on the Texel, Marsen and Arsloe (TMA) spectrum proposed by Holthuijsen (2010). The TMA spectrum derives its name from the TEXEL, MARSEN and ARSLOE datasets that were used by Bouws *et al.* (1985). It is characterised by the product of a JONSWAP (Joint North Sea Wave Observation Project) spectrum $S_J(\omega)$ and a depth factor $H(\omega, h)$

$$S(\omega) = S_J(\omega) \times H(\omega, h). \tag{4.1}$$

The JONSWAP spectrum is defined as

$$S_J(\omega) = S_0 \left(\frac{\omega}{\omega_p}\right)^{-5} \exp\left(-\frac{5}{4}\left(\frac{\omega}{\omega_p}\right)^{-4}\right) \gamma^{\exp\left(-(\omega/\omega_p - 1)^2/(2\sigma_s^2)\right)}, \tag{4.2}$$

where ω_p is the peak angular frequency of the wave field, γ is the peak enhancement factor, $\sigma_s = 0.07$ if $\omega < \omega_p$ and 0.09 otherwise and the constant S_0 is defined implicitly through the relation

$$\int_0^\infty S_J(\omega)\mathrm{d}\omega = \sigma^2 = \langle \eta^2 \rangle, \tag{4.3}$$

where angle brackets denote spatial averaging, $\langle \eta \rangle = 0$ and σ is the standard deviation of the surface elevation. Therefore, the value of S_0 is determined by the characteristic steepness of the wave field, which is expressed as $\varepsilon = 2k_p\sigma$. To transform the deep-water JONSWAP spectrum into a spectrum applicable to arbitrary water depths, the depth factor introduced by Holthuijsen (2010) in (4.1) is defined as

$$H(\omega, h) = \frac{\tanh^2(kh)c}{2c_g}, \quad c_g = \frac{c}{2}\left(1 + \frac{2kh}{\sinh 2kh}\right), \quad c = \frac{\omega}{k}. \tag{4.4}$$

To compare with the wave statistics of Liu *et al.* (2022), we employ the same spectral parameters and numerical resolution across all cases in the present model. The spectral significant wave height is taken as $H_{m0} = 4\sigma = 0.06$ m, with the peak wave period $T_p = 1$ s (corresponding to the peak wavelength $\lambda_p = 1.56$ m, $\omega_p = 2\pi/T_p = 2\pi$ s^{-1} and peak frequency $f_p = 1/T_p = 1$ Hz), and $\gamma = 6$. In the computational set-up, we define the dimensions of the computational domain as $L_x = 128\lambda_p$. The vertical extent of the fluid domain is reduced by using the artificial boundary condition with $b = 1.5H_{m0}$. To discretise the domain, a total of 4096 (horizontal) grid points are used corresponding to 32 points per peak wavelength, coupled with 11 points distributed in the vertical direction. Note that the resolution utilised implies that the spectrum is effectively cut off at $\omega_c \approx 4.86\omega_p$, which is enough for simulating third-order effects, see (3.24) of Klahn *et al.* (2021*b*). Following the same procedure described in Klahn *et al.* (2021*b*,*c*), starting with linearised initial conditions, the nonlinear terms are ramped to fully on over a duration of $10T_p$. Simulations then continue for a total duration of $200T_p$. The characteristic wave

$k_p h$	1	1.5	2	3	4	10
ε	0.1585	0.1334	0.1252	0.1213	0.1208	0.1207
K^+	0.2955	0.1290	0.1200	0.1197	0.1196	0.1195

Table 1. The values of the relative water depth, the characteristic wave steepness and the nonlinear parameter given by (4.5) adopted in the present simulations.
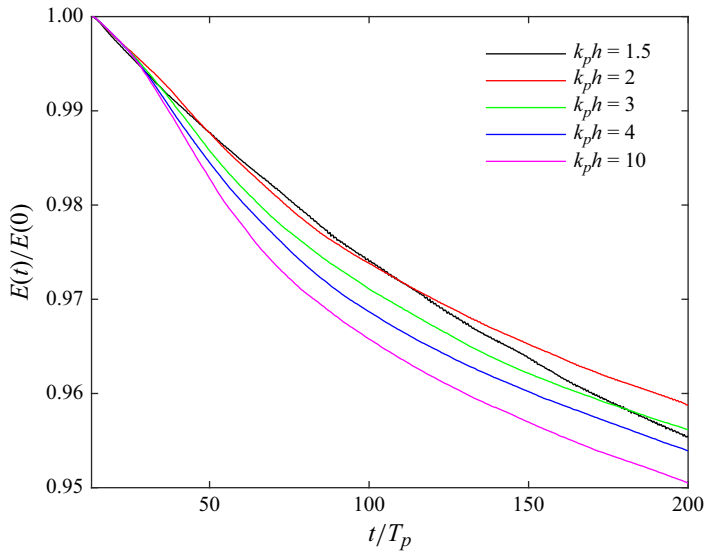

Figure 6. The total mechanical energy as a function of time for wave fields for different values of $k_p h$.

steepness for the linearised initial conditions are set according to ε. To characterise the waves in terms of bound wave nonlinearity, the nonlinear parameter defined by Toffoli *et al.* (2007)

$$K^+ = \frac{H_{m0}k_p}{4}\left(\frac{\left(4\tanh(k_p h)+\tanh(2k_p h)\right)\left(1-\tanh(k_p h)^2\right)}{\tanh(k_p h)\left(2\tanh(k_p h)-\tanh(2k_p h)\right)}+2\tanh(k_p h)\right) \quad (4.5)$$

is used. This parameter transitions to the characteristic steepness as $k_p h \to \infty$ and to the Ursell number as $k_p h \to 0$. The values of $k_p h$, ε and K^+ for each of the cases to be considered are listed in table 1. The time step is set such that $\Delta t = T_p/50$, with artificial damping applied at each time step to ensure stability. For each case, we have carried out the time integration with 500 independent initial conditions, with the phase of each wave component determined randomly. Each individual simulation considered, running on a single processor, requires approximately three hours to complete in terms of wall-clock time. We note that the simulations have thus cumulatively taken approximately one year of computation time in total. Due to the presence of artificial damping, the total energy E, computed according to (3.6), exhibits a gradual decrease of approximately 4 %–5 % over a duration of $200T_p$, as shown in figure 6. This level of energy reduction is comparable in magnitude to that reported by Xiao (2013) and Klahn *et al.* (2021*a*,*b*).
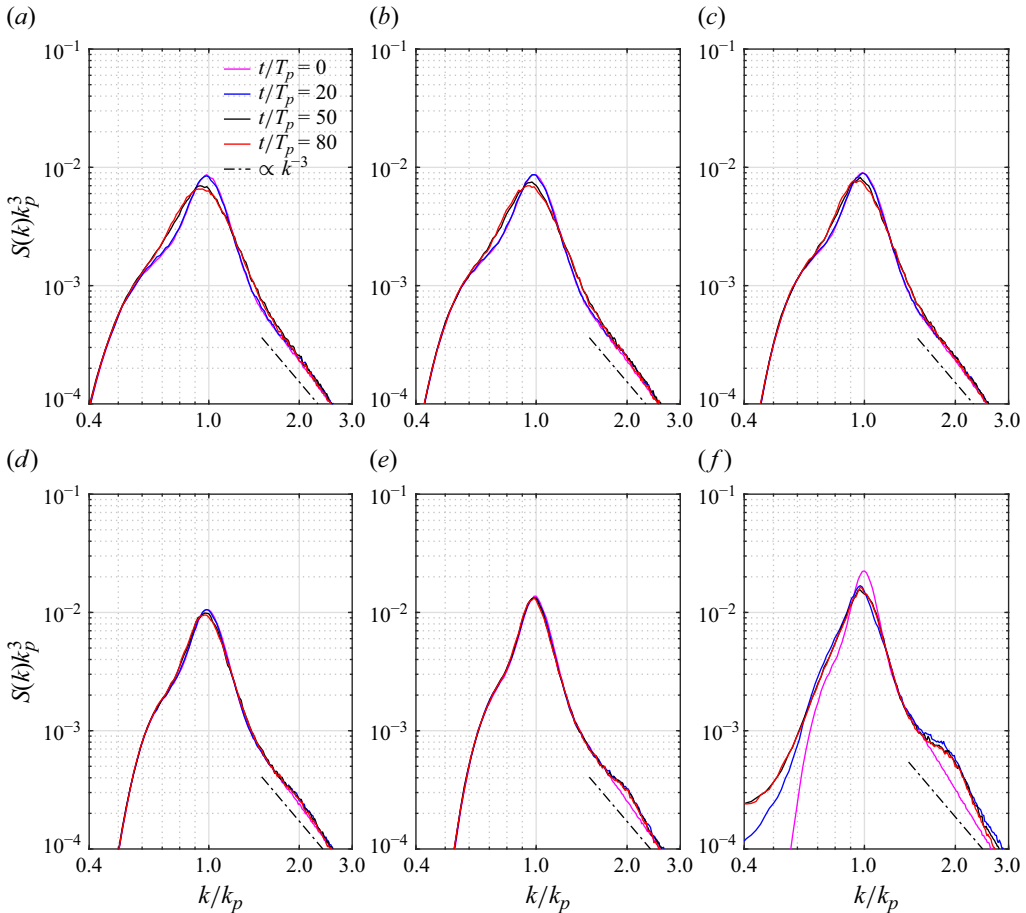
Figure 7. Evolution of the computed spectra for the cases involving six dimensionless water depths.
(a) $k_p h = 10$, (b) $k_p h = 4$, (c) $k_p h = 3$, (d) $k_p h = 2$, (e) $k_p h = 1.5$ and (f) $k_p h = 1$.

4.2. *Wave spectra and significant wave height*

Here, we consider the evolution of the wavenumber spectrum at four different non-dimensional times: $t/T_p = 0$, 20, 50 and 80, as shown in figure 7. Although the total simulation duration is $200T_p$, we present results only up to $80T_p$, as the spectral characteristics exhibit negligible variation beyond approximately $50T_p$, indicating that the spectrum has reached a statistically steady state within the considered wavenumber range. As expected, the initial spectra exhibit minor discrepancies at various water depths due to the change in dispersion relation induced by variation in water depth. As described in Holthuijsen (2010), the derivation of the TMA spectrum depends critically on the assumption that the high-frequency tail of the JONSWAP spectrum in deep water is proportional to f^{-5}. Consequently, the spectrum tail in deep water should be close to the power law k^{-3}, as clearly depicted in figure 7. Similar to previous simulations in finite depth (Xiao 2013), our observations reveal that in deeper water ($k_p h \geqslant 2$, see figure 7a–d), the tails of $S(k)$ are close to k^{-3} and remain time invariant. In shallower water ($k_p h \leqslant 1.5$, see figure 7e, f), the spectral tails at $t/T_p = 0$ are already steeper than k^{-3}. This can be attributed to finite-depth effects, which suppress high-wavenumber (short-wave) components due to enhanced bottom influence and reduced dispersive capacity.
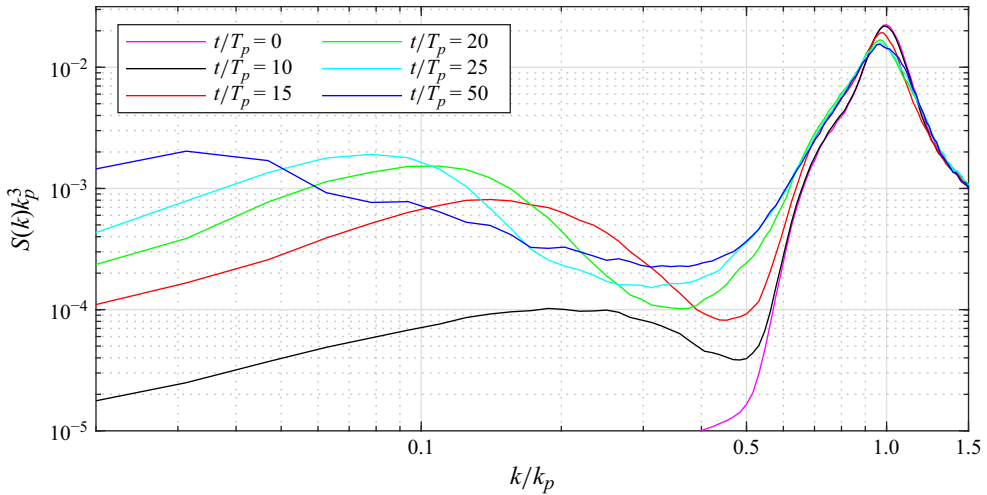
Figure 8. Spectral evolution over time for the case with $k_p h = 1$.

Furthermore, the tails at $t/T_p = 20, 50, 80$ exhibit a steeper slope relative to the initial state at $t/T_p = 0$. A downward shift in the spectral peak is observed in most cases relative to the initial spectrum; however, for $k_p h = 1.5$, the peak frequency remains nearly unchanged. This is because, as $k_p h$ approaches the critical value of 1.363, MI becomes weak and can no longer effectively transfer energy to lower wavenumbers. This finding is in accordance with the results from both experiments conducted by Onorato *et al.* (2009) and numerical simulations presented in Dysthe *et al.* (2003). In these simulation studies, a spectrum shift is already observed on the scale of the Benjamin–Feir instability, and this pattern is also noted in the study of Onorato *et al.* (2002). Furthermore, in the shallowest case ($k_p h = 1$), the peak frequency exhibits a rapid decrease during the initial stage, accompanied by the emergence of a secondary wave system at lower frequencies, as illustrated in figure 8. This is attributed to enhanced nonlinear interactions, which become increasingly effective as dispersion weakens in shallow water.

4.3. *Skewness, kurtosis and the PDF of the surface elevation*

We now investigate some statistical properties of the surface elevation. In figures 9 and 10, we respectively present the skewness $\mathcal{S} = \langle \eta^3 \rangle / \sigma^3$ and kurtosis $\mathcal{K} = \langle \eta^4 \rangle / \sigma^4$ as a function of non-dimensional time in various water depths. As reference the results from Liu *et al.* (2022) are additionally shown in these two figures. As shown in figure 9, $\mathcal{S}$, serving as a descriptor for the vertical asymmetry of the wave profile, increases significantly from the Gaussian value of zero and settles into a relatively steady state of around $\mathcal{S} = 0.2$ over the period of $10T_p$, due to the nonlinear ramping procedure employed in the present simulations. Beyond this time frame, there is a relatively good agreement between the fully nonlinear model and the HOS method adopted in Liu *et al.* (2022), except for the results of $k_p h = 1$, where the fully nonlinear model yields results approximately 25 % higher than those of the HOS method (differences for $t/T_p < 10$ are again due to the ramping procedure employed, and are thus not substantial). Moreover, the stable values are almost constant, even for various $k_p h$. This can be attributed to the similar values of ε for these five cases, see table 1. This is in line with the well-known fact that skewness is proportional to steepness (Fedele & Tayfun 2009).

Kurtosis is predominantly influenced by the nonlinear dynamics of free waves (see e.g. Mori & Janssen 2006; Onorato *et al.* 2009), which plays a crucial role in the generation
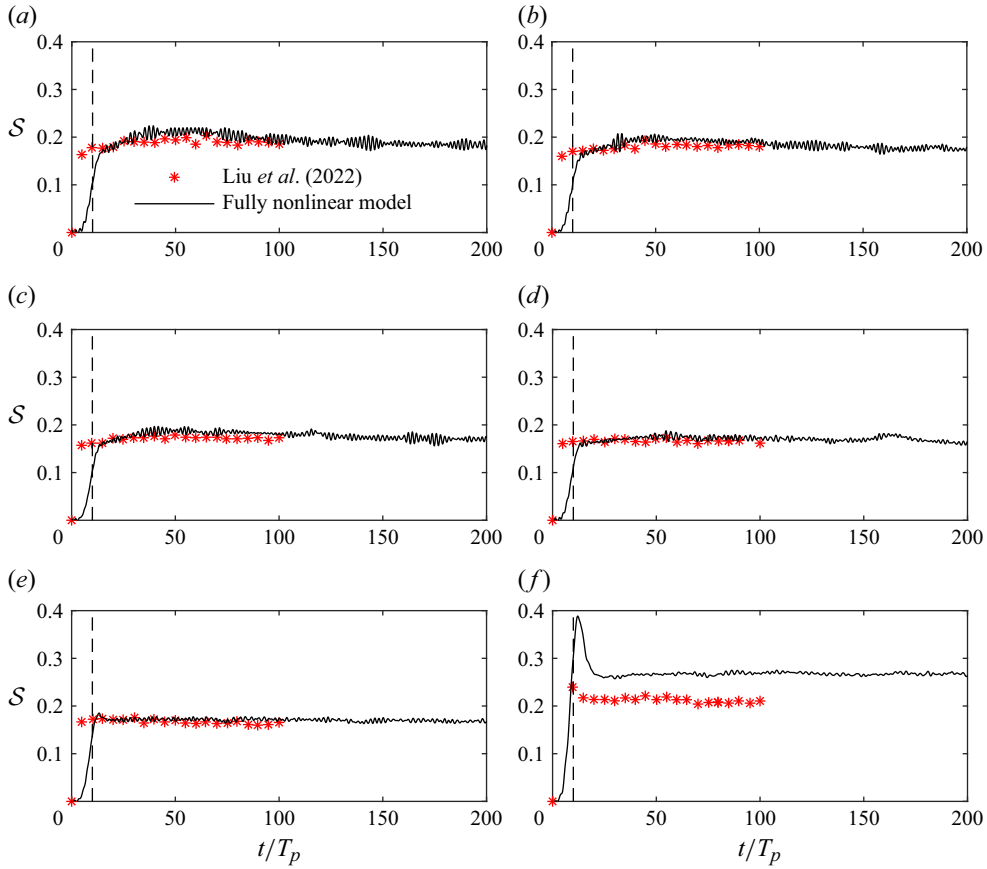
Figure 9. Computed variation of the skewness $\mathcal{S}$ over time with various dimensionless water depths. Asterisks represent HOS results from Liu *et al.* (2022), full lines denote results from the fully nonlinear model and vertical dashed lines indicate the end of nonlinear ramping at $t/T_p = 10$. (a) $k_p h = 10$, (b) $k_p h = 4$, (c) $k_p h = 3$, (d) $k_p h = 2$, (e) $k_p h = 1.5$ and (f) $k_p h = 1$.

of extreme events. The kurtosis $\mathcal{K}$ is regarded to be a good indicator of the importance of MI (see e.g. Xiao *et al.* 2013; Liu *et al.* 2022). The resulting temporal evolution of $\mathcal{K}$ from the fully nonlinear simulations for all five cases are presented as lines in figure 10. In the case of larger water depths (figure 10a–c), it is evident that $\mathcal{K}$ approaches a quasi-steady level after first reaching a local maximum. This indicates that the nonlinear interactions among free waves have been significant in these three scenarios, which has likewise been reported in many studies in deep water (see e.g. Onorato *et al.* 2009; Toffoli *et al.* 2010; Xiao *et al.* 2013). At the instant of maximum $\mathcal{K}$, the wave fields may therefore be considered to be at their most nonlinear state during the simulations. On the other hand, for shallower water depths (figure 10d, e), it is observed that $\mathcal{K}$ converges towards a steady value without necessarily first reaching a clear local maximum. The time at which the roughly steady state is reached depends on water depth. This observation implies that the wave fields considered in these two cases are driven away from their initial Gaussian state by bound wave nonlinearities. It is worth highlighting that, as water depth decreases, the four-wave nonlinear interactions among the free waves become weaker. Assessing all cases considered in this work, it becomes apparent that the quasi-steady value is strongly related to the water depth. More specifically, it tends to be higher for larger water depths.
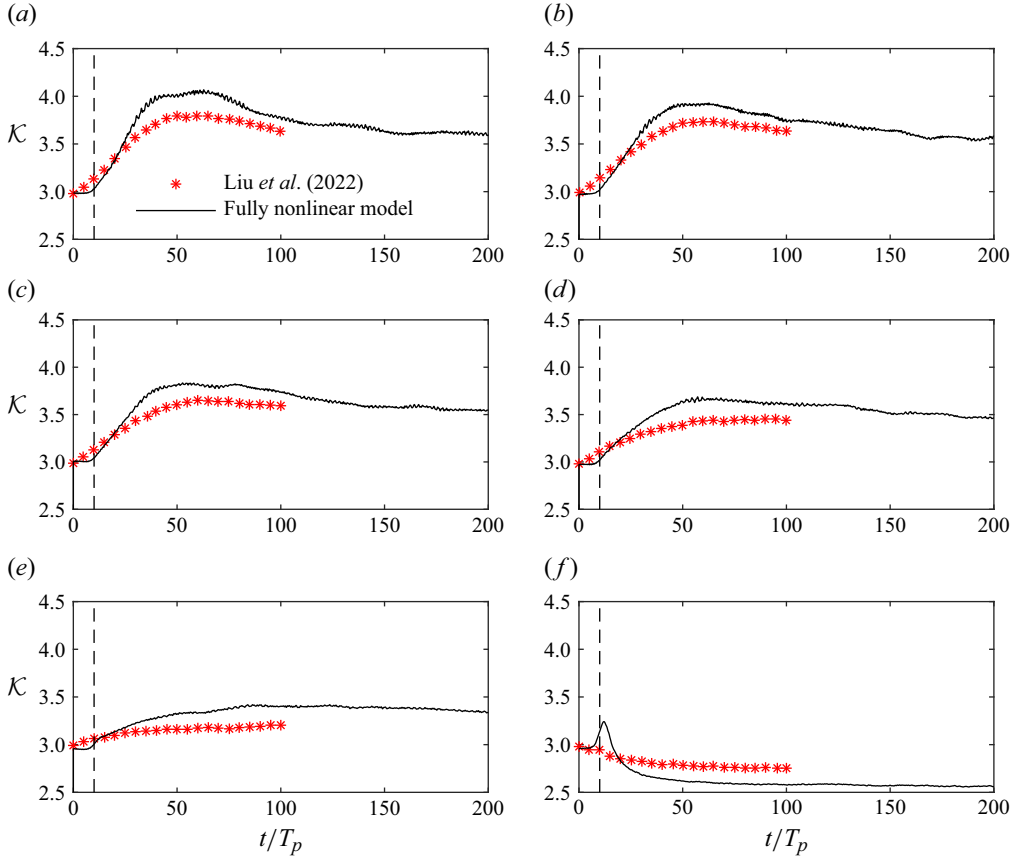
Figure 10. Computed variation of the kurtosis $\mathcal{K}$ over time for various dimensionless water depths. Asterisks represent HOS results from Liu *et al.* (2022), full lines denote results from the fully nonlinear model and vertical dashed lines indicate the end of nonlinear ramping at $t/T_p = 10$. (*a*) $k_p h = 10$, (*b*) $k_p h = 4$, (*c*) $k_p h = 3$, (*d*) $k_p h = 2$, (*e*) $k_p h = 1.5$ and (*f*) $k_p h = 1$.

Compared with the results from Liu *et al.* (2022), the maximum $\mathcal{K}$ from the present fully nonlinear simulations are around 6 % larger, whereas it is approximately 6 % smaller for $k_p h = 1$. This difference can likely be attributed to the presence of full nonlinearity.

We now consider PDFs of the surface elevation at $t/T_p = 50$ for various water depths. The specific time, $t/T_p = 50$, was selected to correspond directly with the results presented by Liu *et al.* (2022). Although PDFs of the surface elevation inherently evolve with time, and thus the choice of the instant analysed could influence quantitative outcomes, adopting $t/T_p = 50$ ensures consistency and facilitates meaningful comparisons. Other instants would likely yield quantitatively distinct distributions, but the chosen reference time provides a robust basis for evaluating and interpreting our results within an established framework. For convenience, we scale the surface elevation η by its standard deviation σ, i.e. as $\zeta = \eta/\sigma$. For each case the numerous space series segments have been collectively analysed, with a ζ bin size corresponding to 0.2, resulting in the six PDFs (circles) shown in figure 11. Error bars are also included, estimated as $\pm p(\zeta)/\sqrt{N_b}$, where N_b is the number of samples in each bin, following Onorato *et al.* (2009). Also shown for comparison are the PDFs from (i) the third-order HOS results of Liu *et al.*
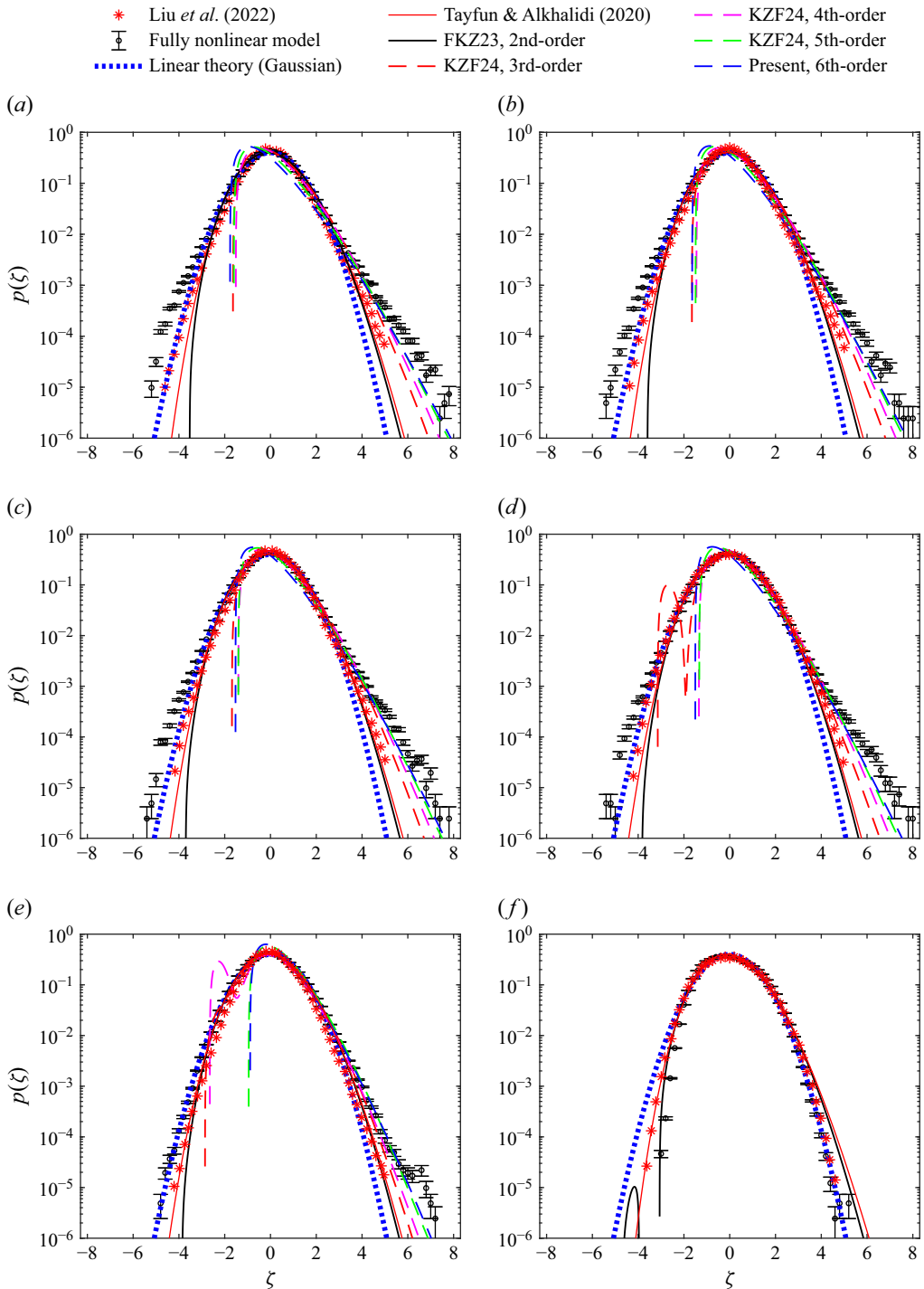
Figure 11. Comparison of PDFs computed from data generated using the present fully nonlinear model (Klahn *et al.* 2021*d*, circles, with error bars) with simulated results from the third-order HOS method (Liu *et al.* 2022, asterisks), second-order theory (Fuhrman *et al.* 2023, black lines, referred to as FKZ23; Tayfun & Alkhalidi 2020, red lines), as well as third- through sixth-order theoretical solutions (dashed lines, following the methodology of Klahn *et al.* 2024, referred to as KZF24 above). (*a*) $k_p h = 10$, (*b*) $k_p h = 4$, (*c*) $k_p h = 3$, (*d*) $k_p h = 2$, (*e*) $k_p h = 1.5$ and (*f*) $k_p h = 1$.

(2022) (asterisks), (ii) the (first-order) Gaussian distribution (dotted lines)

$$p(\zeta) = \frac{1}{\sqrt{2\pi}} \exp\left(-\frac{\zeta^2}{2}\right), \tag{4.6}$$

and (iii) the exact second-order theoretical PDF derived recently by Fuhrman *et al.* (2023) (black lines)

$$p(\zeta) = \left(\frac{2}{\mathcal{S}}\right)^{1/3} \exp\left[\frac{1}{3\mathcal{S}^2} + \frac{\zeta}{\mathcal{S}}\right] Zi\,(\chi), \tag{4.7}$$

where

$$\chi = \left(\frac{2}{\mathcal{S}}\right)^{1/3} \left(\frac{1}{2\mathcal{S}} + \zeta\right), \tag{4.8}$$

$$Zi(\chi) \equiv \begin{cases} Ai(\chi) & \text{for } \chi \geqslant -1.17371, \\ Ci(\chi) & \text{for } \chi < -1.17371, \end{cases} \tag{4.9}$$

where

$$Ci(\chi) \equiv [Ai(\chi)^2 + Bi(\chi)^2]^{1/2}. \tag{4.10}$$

Note that the switch to the $Ci(\chi)$ function in (4.9) below the indicated threshold for χ was suggested by Fuhrman *et al.* (2023), provided that $\mathcal{S} \leqslant 0.2$, to eliminate non-physical oscillatory behaviour for negative ζ in the otherwise theoretical solution. Above, $Ai(\chi)$ and $Bi(\chi)$ are respectively the Airy functions of the first and second kinds. Figure 11 also presents (iv) the second-order Tayfun & Alkhalidi (2020) distribution (red lines)

$$p(\zeta) = \begin{cases} \alpha p_G(\zeta_s)/(1 + \epsilon_1 \zeta_s) & \text{for } \zeta_s > 0, \\ \alpha p_G(\zeta_s)/\exp(\epsilon_1 \zeta_s) & \text{for } -2/\epsilon_1 < \zeta_s \leqslant 0, \\ 0 & \text{for } \zeta_s \leqslant -2/\epsilon_1, \end{cases} \tag{4.11}$$

where

$$\zeta = \begin{cases} (\zeta_s + \epsilon_1 \zeta_s^2/2 - \eta_m)/\sigma_s & \text{for } \zeta_s > 0, \\ (\zeta_s e^{\epsilon_1 \zeta_s/2} - \eta_m)/\sigma_s & \text{for } -2/\epsilon_1 < \zeta_s \leqslant 0, \end{cases} \tag{4.12}$$

where $\alpha = \sigma_s/P_G(2/\epsilon_1)$, p_G is the standard normal PDF, see (4.6), P_G is the standard normal cumulative distribution function, $\epsilon_1 = 0.3377\mathcal{S} + 0.0174\mathcal{S}^2 + 0.0259\mathcal{S}^3$, $\eta_m = 0.1687\mathcal{S} - 0.0012\mathcal{S}^2 + 0.0101\mathcal{S}^3$ and $\sigma_s = 1 + 0.0025\mathcal{S} + 0.0396\mathcal{S}^2 + 0.0104\mathcal{S}^3$. Additionally shown in figure 11 are (v) numerically determined PDFs at third- through sixth-order, based on the theoretically based solutions of Klahn, Zhai & Fuhrman (2024), who showed that the theoretical PDFs could be computed to essentially any desired order, which was newly posed as solutions to an ordinary differential equation. The sixth-order results based on their methodology are newly presented in this study, with the required coefficients used in the solution detailed in Appendix A. The statistical moments required for the calculation of the second- through sixth-order theoretical PDFs are as indicated in table 2, calculated from all model results at $t/T_p = 50$. Space series of the surface elevation containing the largest computed rogue waves are likewise provided in figure 12, as examples, where it is seen that these rogue waves often appear to be surrounded by an otherwise rather ordinary wave field for the given conditions. From these PDFs, as well

$k_p h$	$\mathcal{S}$	$\mathcal{K}$	$\mathcal{S}_h = \langle \zeta^5 \rangle$	$\mathcal{K}_h = \langle \zeta^6 \rangle$	$m_7 = \langle \zeta^7 \rangle$
1	0.2679	2.624	2.060	10.99	15.89
1.5	0.1775	3.341	2.324	22.04	37.82
2	0.1796	3.667	2.937	30.32	64.52
3	0.1894	3.800	3.199	32.65	69.19
4	0.1991	3.907	3.481	35.23	79.40
10	0.2051	4.044	3.760	38.91	90.26

Table 2. Summary statistical moments of cases considered in the present work ($\mathcal{S}_h$ is the hyperskewness, $\mathcal{K}_h$ is the hyperkurtosis and m_7 is the seventh statistical moment).

as the depicted space series, it is seen that all fully nonlinear simulations result in isolated rogue waves, with crest elevations in the most extreme cases reaching nearly $\zeta = 8$ i.e. eight standard deviations above the mean.

From figure 11, it is observed that the third-order HOS results of Liu *et al.* (2022) exhibit noticeable deviations from the present fully nonlinear results, which generally predict significantly increased probability density of both extreme wave crests and troughs, as is clear in both positive and negative tail regions. It is well known that, as $k_p h$ approaches 1.363, the four-wave nonlinear interactions (in the weakly nonlinear regime, at least within the narrow-band approximation) become weaker. Therefore, the two primary factors contributing to this observed discrepancy are seemingly limitations associated with higher-order nonlinear dynamics of free waves and stronger effects arising from bound waves. Additionally, we further observe that none of the current theoretical distributions fully capture the characteristics of the simulated results. To illustrate this, we proceed by comparing our findings with a range of analytical distributions, detailing how each aligns with or diverges from the simulated outcomes. Notably, the heavy positive tailed regions computed from the present fully nonlinear results are reasonably predicted by e.g. the fifth and sixth-order solutions based on Klahn *et al.* (2024), although even these under-predict the probability density in these regions, perhaps with the exception of results with $k_p h = 1.5$. This stands in contrast to the findings of Toffoli *et al.* (2007), who reported no significant deviations from second-order theory. The discrepancy is likely attributable to the fact that their data are characterised by a directional spreading, whereas our computations are based on long-crested, unidirectional waves, which represent an idealised scenario providing an upper bound for wave statistics. On the other hand, none of the depicted theoretical PDFs do an adequate job of predicting the probability density of the negative tail region (where the resulting theoretical PDFs turn oscillatory at third and higher orders), which is considered as an open problem. Furthermore, at $k_p h = 1$, $\mathcal{K}$ is 2.6244 (see table 2), which is less than 3. Therefore, the theoretical PDFs above second order proposed by Klahn *et al.* (2024) are not applicable (and hence not shown), as cumulants used in their theory should be positive.

4.4. *Wave crest distribution and rogue wave occurrence*

Here, we investigate the exceedance probability of the wave crest, defined as the highest elevation of each individual wave with respect to the mean water level using zero-up crossing analysis. In the context of the crest amplitude, linear theory predicts a Rayleigh distribution

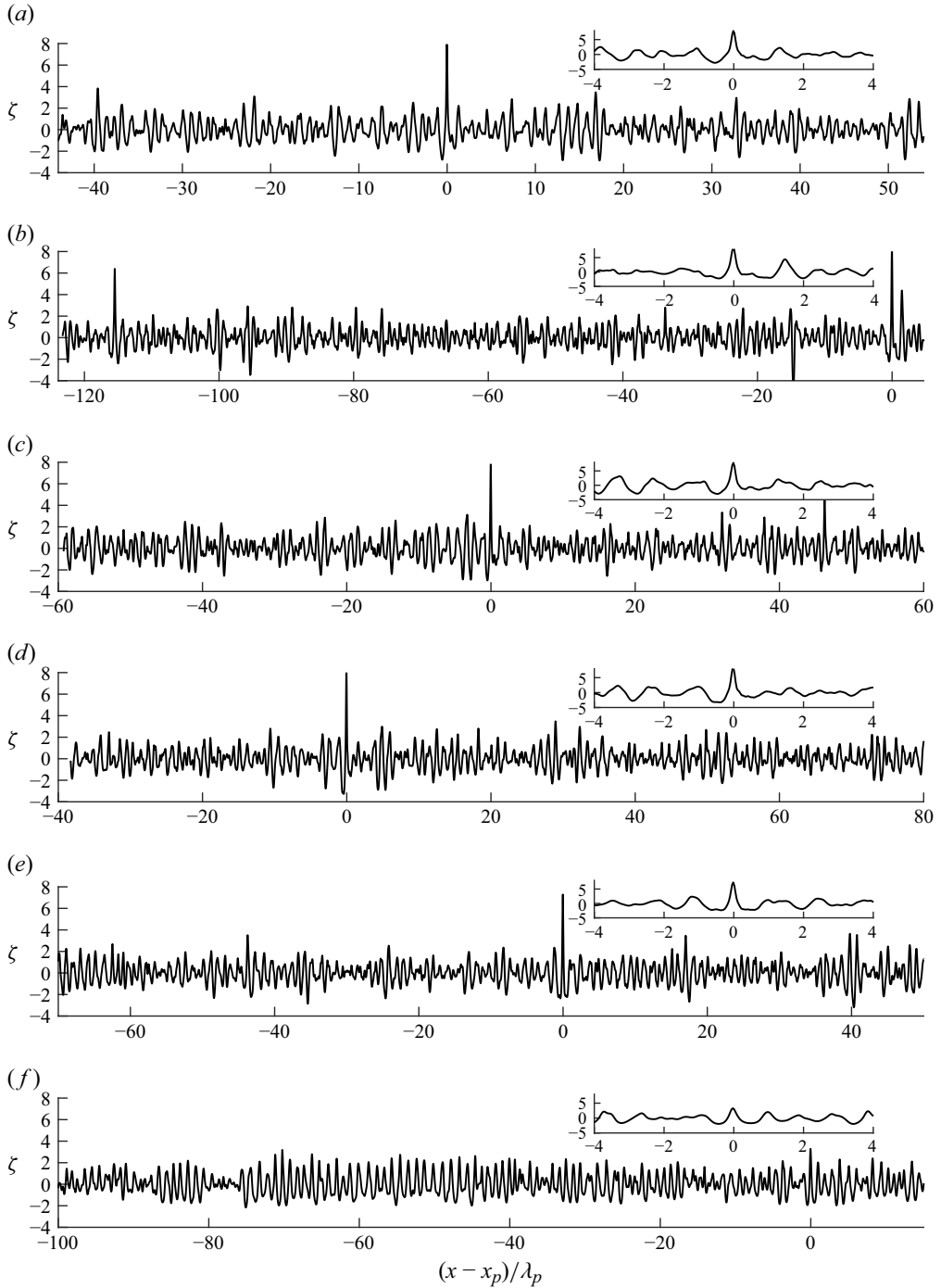$$P \left(\frac{\eta_c}{H_{m0}} \right) = \exp \left(-8 \frac{\eta_c^2}{H_{m0}^2} \right), \tag{4.13}$$

Figure 12. Example snapshots of the computed surface elevation surrounding the largest crests generated by the fully nonlinear wave model of Klahn *et al.* (2021*c*). Insets depict the region immediately surrounding the largest crest. Variable x_p denotes the x position of the highest crest. (*a*) $k_p h = 10$, (*b*) $k_p h = 4$, (*c*) $k_p h = 3$, (*d*) $k_p h = 2$, (*e*) $k_p h = 1.5$ and (*f*) $k_p h = 1$.

whereas second-order interactions should play a role in causing deviations from this result. Assuming deep water and narrow-bandedness of the spectrum, Tayfun (1980) formulated a second-order wave crest distribution, which is also reasonably suitable in intermediate water depth according to Fedele *et al.* (2019). The exceedance probability is expressed as

$$P\left(\frac{\eta_c}{H_{m0}}\right) = \exp\left[-\frac{8}{H_{m0}^2 k_p^2}\left(\sqrt{1 + 2k_p\eta_c} - 1\right)^2\right] = \exp\left[-\frac{2}{\varepsilon^2}\left(\sqrt{1 + 4\varepsilon\frac{\eta_c}{H_{m0}}} - 1\right)^2\right],$$
(4.14)

where η_c is the crest height. Extending this framework, Tayfun & Fedele (2007) later proposed a third-order wave crest distribution model, further improving the description of nonlinearity

$$P\left(\frac{\eta_c}{H_{m0}}\right) = \exp\left[-\frac{2}{\varepsilon^2}\left(\sqrt{1 + 4\varepsilon\frac{\eta_c}{H_{m0}}} - 1\right)^2\right]\left[1 + \Lambda\left(\frac{\eta_c}{H_{m0}}\right)^2\left(\left(\frac{2\eta_c}{H_{m0}}\right)^2 - 1\right)\right],$$
(4.15)

where $\Lambda = \lambda_{40} + 2\lambda_{22} + \lambda_{04}$ is a relative measure of third-order nonlinearities. The surface cumulants λ_{mn} are defined by

$$\lambda_{mn} = \frac{\langle\eta^m\hat{\eta}^n\rangle}{\sigma^{m+n}} + (-1)^{m/2}(m-1)(n-1), \quad \text{for} \quad m+n = 4,$$
(4.16)

where $\hat{\eta}$ is the Hilbert transform of η. In figure 13, the theoretical (linear) Rayleigh, second-order Tayfun and third-order Tayfun–Fedele distributions, along with the simulated results of Liu *et al.* (2022), are utilised as references for comparing with the numerical results obtained from the present fully nonlinear model at $t/T_p = 50$.

The wave crest distributions from the present fully nonlinear simulations exhibit a substantial departure from the Tayfun distribution (4.14) at the tails for cases having larger water depths (see figure 13a–d), although this solution still notably provides much better accuracy than the Rayleigh distribution. These deviations are primarily influenced by the nonlinear dynamics of free waves, which dominates the statistical characteristics of the wave crests. The aforementioned phenomenon of deviation from the Tayfun distribution has already been substantiated in the context of long–crested waves through experimental and numerical models, as demonstrated in Onorato *et al.* (2006) and Onorato *et al.* (2009). As we move towards shallower water depth (see figure 13e), the crest amplitude attenuates, leading to reduced (but still apparent) deviations from the second-order theory. Similar trends with respect to water depth are also observed in the simulations conducted by Liu *et al.* (2022), confirming that the primary contributing factor is likely the MI enhanced by third-order nonlinearity. For each case considered in the present work, comparing with the third-order HOS simulation results of Liu *et al.* (2022), the results of the fully nonlinear simulations demonstrate much larger probability of large crests, especially for $k_p h \geqslant 1.5$. This discrepancy can be attributed to the impact of full nonlinearity in the interactions among free waves, which will result in and enhance the MI. It should be noted that, at $k_p h = 1.5$, Liu *et al.* (2022) showed that the difference between their results and the second-order Tayfun distribution almost disappears, which indicates that their simulated wave fields are dominated by bound wave effects. Conversely, the deviation of the present results from both the Tayfun and Tayfun–Fedele distributions is still significant. This seemingly indicates that the nonlinear dynamics of free waves and higher-order bound wave effects remain important in the statistical properties of the fully nonlinear wave fields. The third-order Tayfun–Fedele model yields improved predictions in the tail
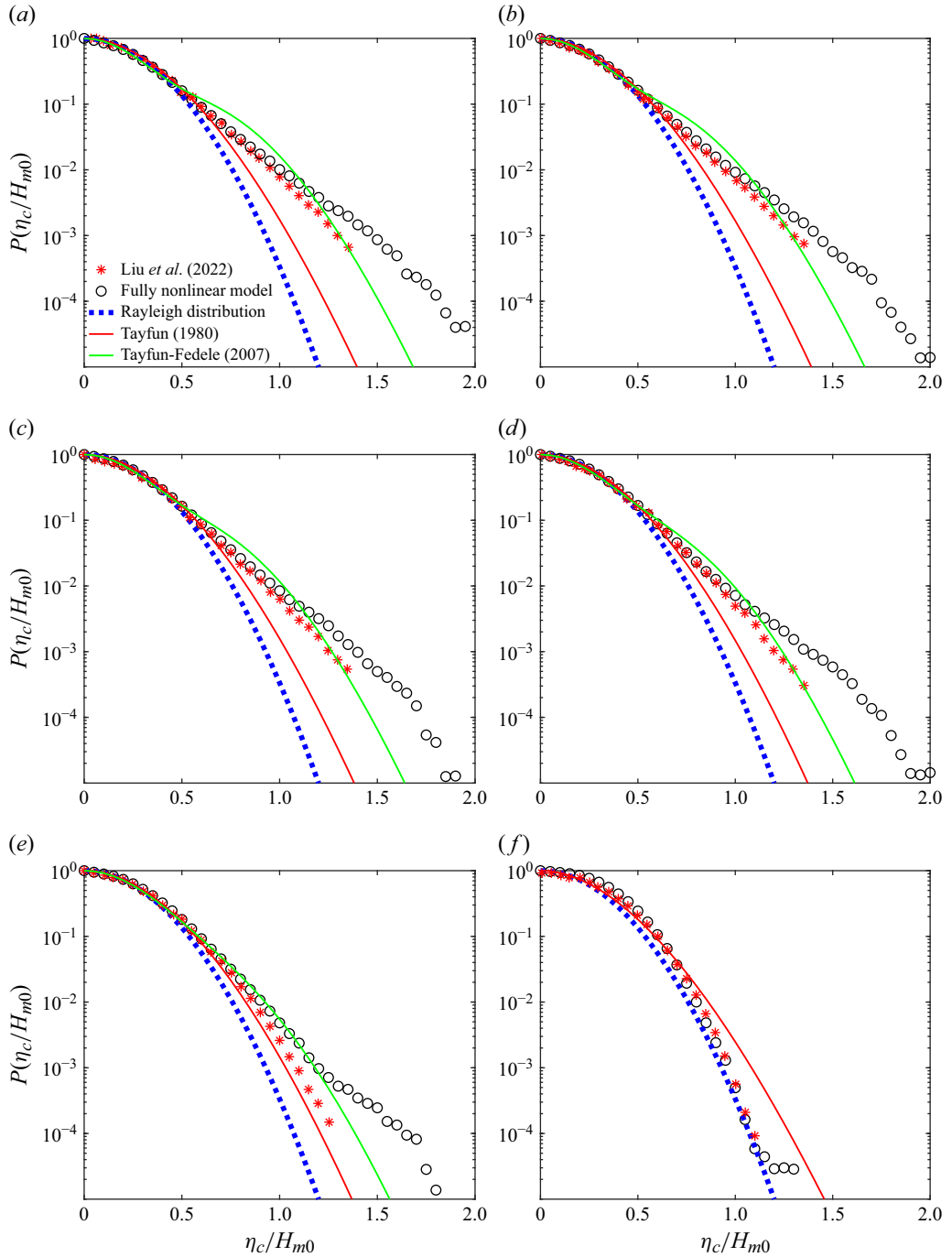
Figure 13. Exceedance probability of wave crests for various dimensionless depths $k_p h$. Also shown are the Rayleigh distribution (dotted lines), the second-order Tayfun distribution (full lines), results from the third-order HOS model from Liu *et al.* (2022) (asterisks) and those from the present fully nonlinear simulations (circles). (*a*) $k_p h = 10$, (*b*) $k_p h = 4$, (*c*) $k_p h = 3$, (*d*) $k_p h = 2$, (*e*) $k_p h = 1.5$ and (*f*) $k_p h = 1$.

region compared with the second-order Tayfun model. However, it still underestimates the probability of extreme crests when compared with fully nonlinear simulations. This highlights the limitations of weakly nonlinear approximations in capturing the strongly nonlinear wave dynamics, consistent with the findings of Karmpadakis, Swan & Christou (2019). Furthermore, at $k_p h = 1$, λ_{40} takes a negative value (-0.3756), which violates the underlying assumption of the Tayfun–Fedele model that λ_{40} must be positive. As such, the model is not applicable in this case and is therefore omitted.

The simplest rogue wave definition is one having $\eta_c > 1.25H_{m0}$. Figure 14 depicts the progression of the probability of rogue wave occurrence $P(\eta_c > 1.25H_{m0})$ for various dimensionless water depths. As observed, both the present model and the HOS method truncated at third order reveal an initial increase in $P(\eta_c > 1.25H_{m0})$, attributed to the robust MI of the wave fields. Subsequently, a decline ensues, and eventually a relatively stable stage will occur if the simulation is sufficiently long. Here, we focus on comparing the present results with those obtained using the third-order HOS method (Liu *et al.* 2022). Notably, the present model exhibits a more rapid increase during the ascending phase. ($20 \leqslant t/T_p \leqslant 50$) and produces higher $P(\eta_c > 1.25H_{m0})$ values compared with the third-order HOS results, albeit of the same order of magnitude. For instance, in the deepest case with $k_p h = 10$, the maximum $P(\eta_c > 1.25H_{m0})$ reaches up to 2.93×10^{-3}, significantly exceeding the third-order HOS (Liu *et al.* 2022) peak of 1.68×10^{-3} by nearly a factor of two. This highlights the discernible impact of full nonlinearity on MI, further contributing to the likelihood of rogue wave formation. As the depth $k_p h$ decreases from 10 to 1.5, both the initial growth rate and $P(\eta_c > 1.25H_{m0})$ decrease, yet the maximum values still significantly exceed the third-order HOS predictions. This further illustrates that the MI induced by the higher-order nonlinearity weakens as water depth decreases.

The time evolution of $P(\eta_c > 1.25H_{m0})$ and $\mathcal{K}$ is plotted simultaneously in figure 14 to enable comparison and analysis of their relationship. This comparison reveals that the evolution of $P(\eta_c > 1.25H_{m0})$ is consistent with that of $\mathcal{K}$. This connection emerges as the kurtosis is closely tied to MI, serving as a primary indicator for the occurrence of rogue waves. Kurtosis as such an indicator has been widely used in deep water (e.g. Mori & Janssen 2006; Xiao *et al.* 2013). To better elucidate and quantify the relationship in finite depth, we plot $P(\eta_c > 1.25H_{m0})$ for various water depths at distinct times (ranging from $t = 10T_p$ to $100T_p$ in $5T_p$ increments) as a function of the excess kurtosis $\mathcal{K} - 3$ in figure 15. Based on these scatter distributions, we compute a linear fit

$$P(\eta_c > 1.25H_{m0}) = 0.0026(\mathcal{K} - 3), \tag{4.17}$$

with a coefficient of determination (R^2) of approximately 0.93 from the fully nonlinear model, surpassing the value obtained from the third-order HOS results of Liu *et al.* (2022), who found the fit

$$P(\eta_c > 1.25H_{m0}) = 0.0010(\mathcal{K} - 3), \tag{4.18}$$

with $R^2 = 0.56$ based on their results. This indicates that the present model gives a stronger correlation than the third-order HOS method. Comparison of (4.17) and (4.18) indicates that full nonlinearity increases the probability of rogue waves for a given excess kurtosis by a factor $0.0026/0.0010 = 2.60$ for the present conditions.

5. Dependence of kurtosis on BFI

The results presented above highlight the potential substantial influence of MI in finite water depths i.e. down to $k_p h = 1.5$. Additionally, they emphasise that kurtosis serves as a
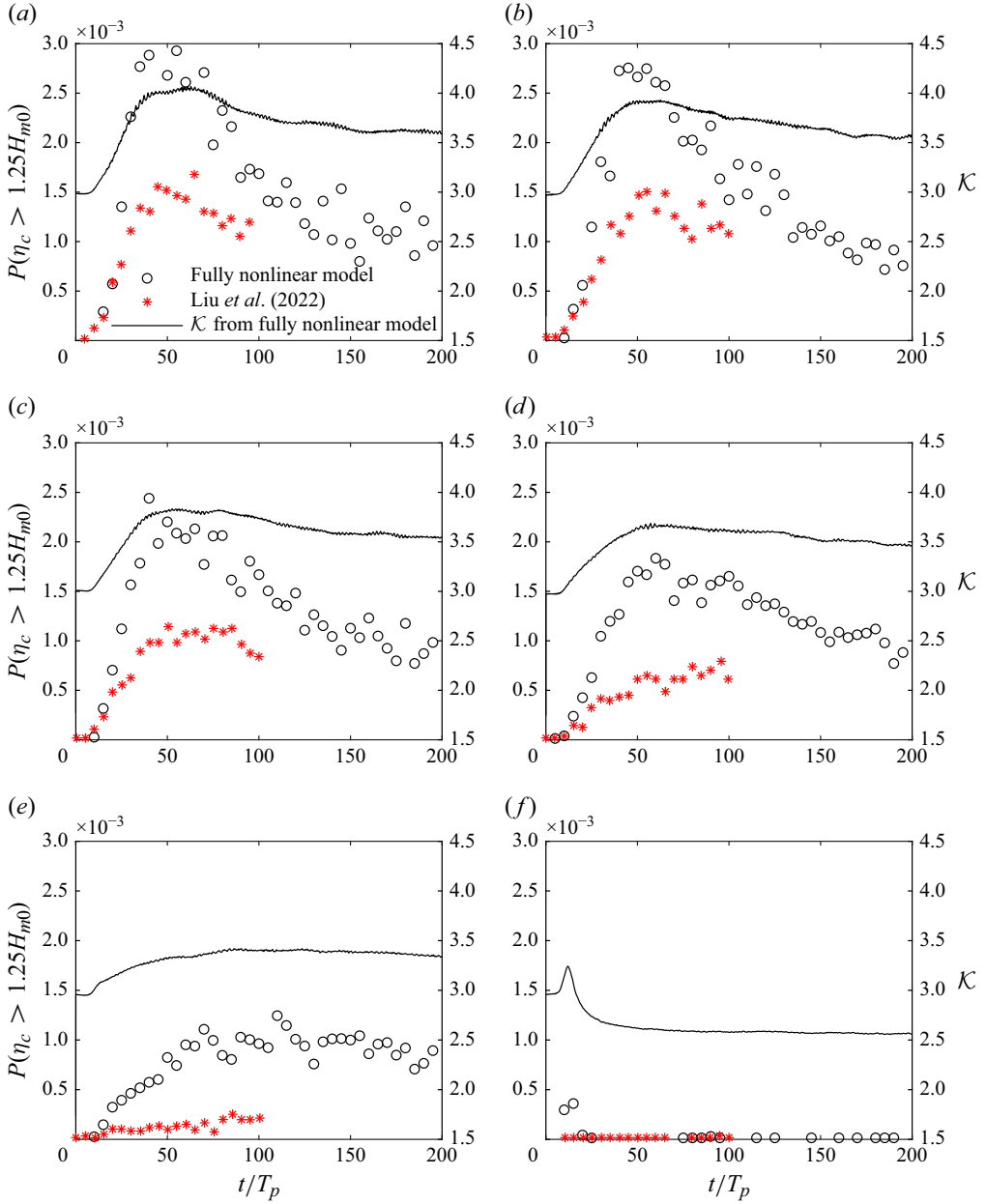
Figure 14. Comparison of the probability of rogue wave occurrence from the fully nonlinear model (circles) with third-order HOS results reported in Liu *et al.* (2022) (asterisks). (*a*) $k_p h = 10$, (*b*) $k_p h = 4$, (*c*) $k_p h = 3$, (*d*) $k_p h = 2$, (*e*) $k_p h = 1.5$ and (*f*) $k_p h = 1$.

reliable indicator for both MI and the occurrence of rogue waves. Nevertheless, obtaining the kurtosis value directly from the wave spectrum poses a challenge. Consequently, the widely adopted approach for evaluating the impact of MI based on the wave spectrum is the use of the BFI. For finite water depths, BFI $= \rho \varepsilon_0 / \delta_\omega$ (Janssen & Bidlot 2009), where $\varepsilon_0 = 2 H_{m0} k_{p0}$, $k_{p0} = \omega_p^2 / g$ and
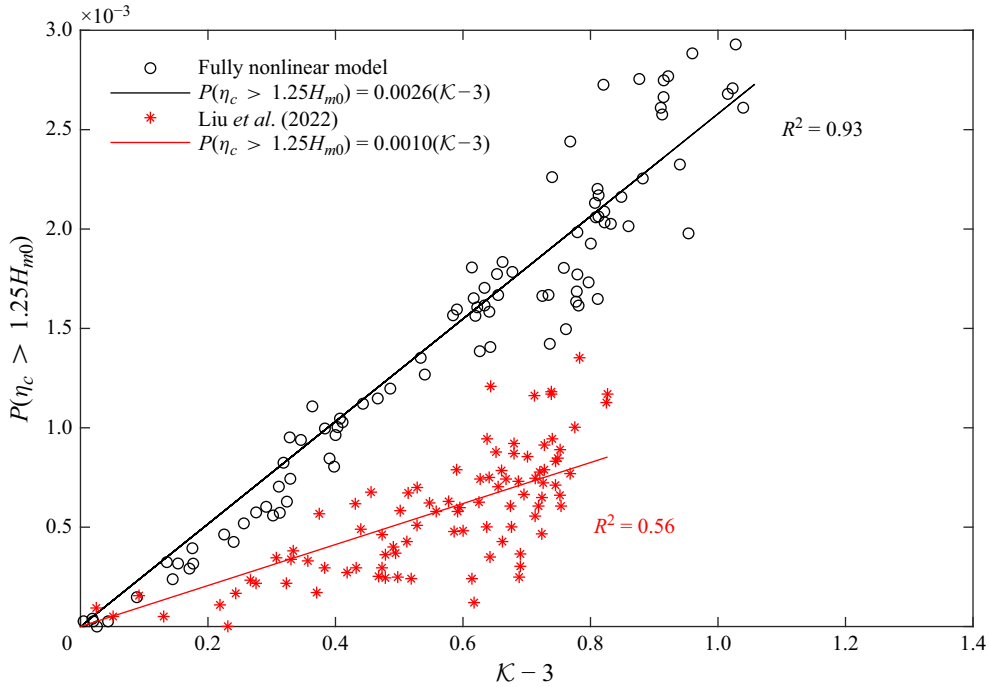
Figure 15. Correlation between the probability of rogue wave occurrence $P(\eta_c > 1.25H_{m0})$ and the excess kurtosis $\mathcal{K} - 3$. Depicted are results from third-order HOS modelling of Liu *et al.* (2022) (asterisks) and the present fully nonlinear simulations (circles), with best-fit lines shown for both.

$$\delta_\omega = \frac{1}{\sqrt{\pi}\left(-0.015\gamma^2 + 0.6\gamma + 1.37\right)} \tag{5.1}$$

is the spectral bandwidth, while

$$\rho = Re\left[\sqrt{\frac{gT_{1111}}{k_p^4 \omega_p \omega_p''(k)}}\right]\frac{c_g}{c} \tag{5.2}$$

is the depth factor. In finite water depths, T_{1111} and the second derivative of angular frequency with respect to wavenumber $\omega_p''(k)$ are calculated using the expressions of Janssen & Onorato (2007)

$$\frac{T_{1111}}{k_p^3} = \frac{9T_1^4 - 10T_1^2 + 9}{8T_1^3} - \frac{1}{k_p h}\left[\frac{\left(2c_g - c/2\right)^2}{gh - c_g^2} + 1\right], \tag{5.3}$$

$$\omega_p''(k) = -\frac{g\left(\left(T_1 - k_p h\left(1 - T_1^2\right)\right)^2 + 4\left(k_p h\right)^2 T_1^2\left(1 - T_1^2\right)\right)}{4\omega_p k_p T_1}, \tag{5.4}$$

where $T_1 = \tanh(k_p h)$. In this context, we investigate the BFI as a reliable indicator of the relationship between full nonlinearity and the occurrence probability of rogue waves. The BFI and aforementioned K^+ (see § 4.1) are both functions of $k_p h$ by definition. These two parameters are associated with free wave and bound wave nonlinearity, respectively. Therefore, we plot the dependence of these two parameters on $k_p h$ in figure 16 for the wave conditions described in § 4.1 to illustrate how the relative importance of bound and free wave nonlinearity evolves with $k_p h$. Note that free wave effects become dominant
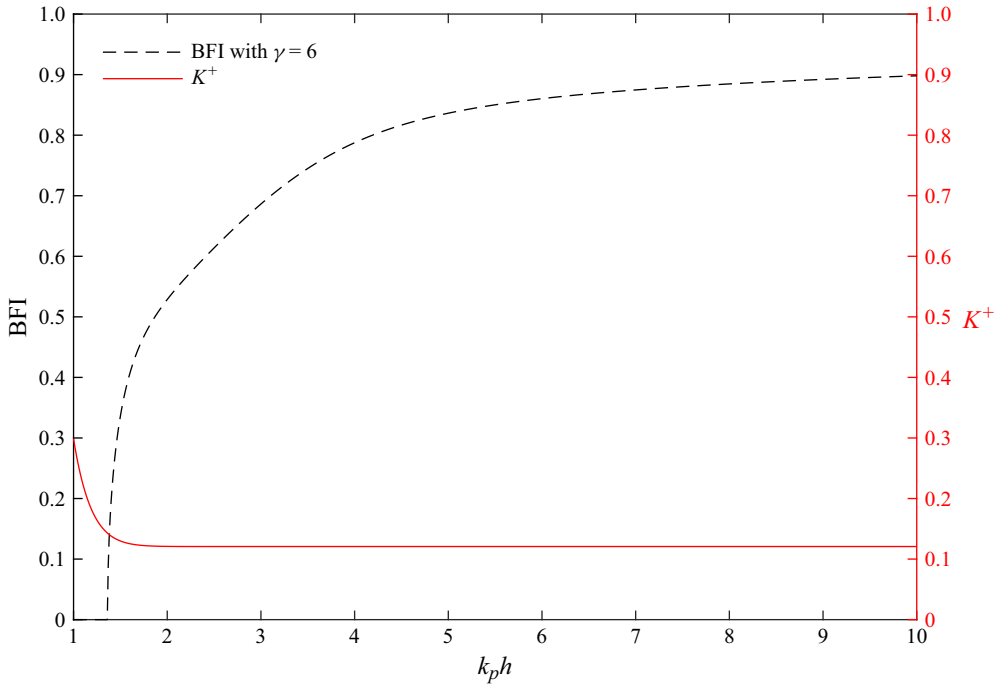
Figure 16. The dependence of BFI and K^+ on $k_p h$ for waves with $T_p = 1$ s, $\lambda_p = 1.56$ m, $H_{m0} = 0.06$ m and $\gamma = 6$. Depicted are results of BFI (dash line) and K^+ (full line).

in deeper water conditions. In contrast, bound wave effects dominate in shallower water depths where $k_p h < 1.363$. Various researchers have explored the relationship between $\mathcal{K}$ and BFI. These investigations encompass theoretical analysis, numerical simulations and experimental studies. Mori & Janssen (2006) proposed that , for unidirectional deep-water wave fields under the assumption of a narrow-band and stationary spectrum, the long-time value of $\mathcal{K}$ is proportional to BFI^2. For non-stationary wave fields, Onorato *et al.* (2016) related the evolution of kurtosis to variations in spectral bandwidth; however, their framework does not provide predictions for $\mathcal{K}_{max}$ observed under transient conditions. The correlation between $\mathcal{K}_{max}$ and BFI in finite-depth simulations, based on the third-order HOS method (Liu *et al.* 2022), similarly found that $(\mathcal{K}_{max} - 3)$ is proportional to BFI^2. The aforementioned findings clearly indicate that BFI serves as an effective indicator of the impact of third-order nonlinearity in the wave field. However, the influence of full nonlinearity on the correlation between the BFI and statistical measures such as kurtosis in finite water depth remains unclear. Hence, to explore this relationship, we employ the present fully nonlinear model to simulate unidirectional wave fields with initial TMA spectra covering a broader range of frequency bandwidths (i.e. $\gamma = 1$, 1.5, 3, 6 and 9) and water depths ($k_p h = 1.5$, 2, 3, 4 and 10), amounting to a total of 25 tested cases. For each case, we have carried out 500 realisations with a total simulated duration of $200 T_p$, each characterised by initially independent and random phases, as before. The results are depicted in figure 17. In contrast to previously reported results that $(\mathcal{K}_{max} - 3) \propto BFI^2$ for weakly nonlinear deep-water waves, a linear correlation is found, corresponding to

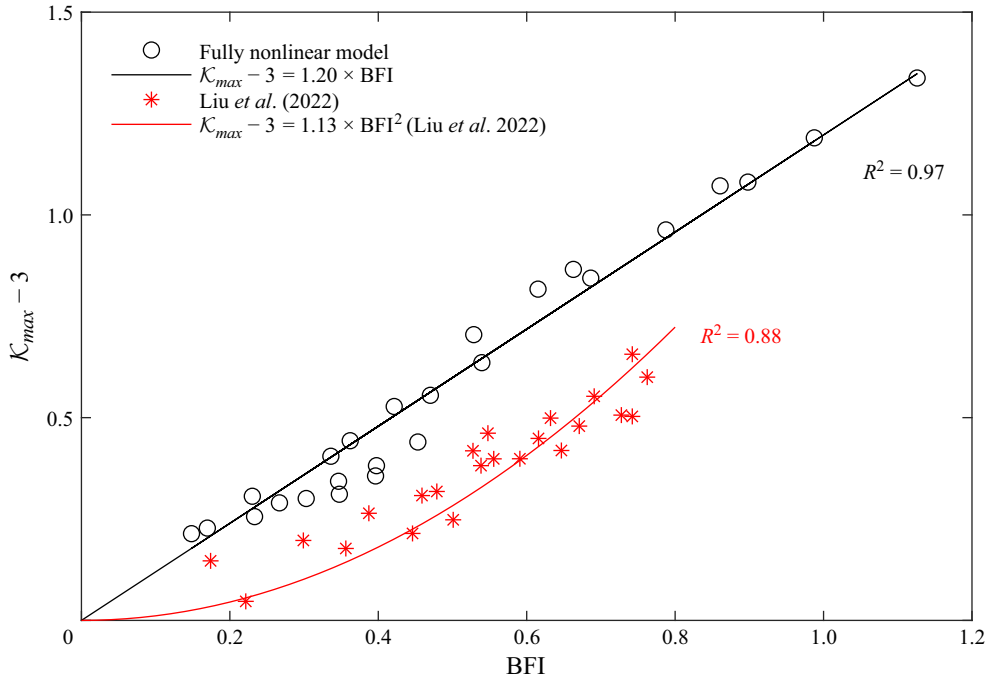$$\mathcal{K}_{max} - 3 = 1.20 \times BFI, \qquad (5.5)$$

Figure 17. The dependence of the maximum kurtosis on BFI. Depicted are results from third-order HOS modelling of Liu *et al.* (2022) (asterisks) and the present fully nonlinear simulations (circles). The black line represents the best fit to the present (fully nonlinear model) data whereas the red line corresponds to the curve based on third-order HOS results, as suggested by Liu *et al.* (2022) (there found by plotting ($\mathcal{K}_{max} - 3$) vs. BFI^2 rather than as above).

with coefficient of determination $R^2 = 0.97$ being very near unity and surpassing the value of $R^2 = 0.88$ reported in Liu *et al.* (2022), based on their quadratic fit

$$\mathcal{K}_{max} - 3 = 1.13 \times \text{BFI}^2. \tag{5.6}$$

This means that the fitted values have a stronger correlation with the observed values when compared with the results presents in Liu *et al.* (2022). Furthermore, when plotted as in figure 17, it is clear that a linear relationship is also supported by the third-order HOS data of Liu *et al.* (2022), similar to the present finding. This suggests that the data from Liu *et al.* (2022) are adequately represented by a linear fit, while the adoption of a quadratic form is not theoretically justified. The extension to higher BFI values in figure 17 is primarily due to the inclusion of deep-water conditions ($k_p h = 10$) in the present study, in contrast to the shallower range ($k_p h \leqslant 4$) considered by Liu *et al.* (2022). It is therefore reasonable to expect that, if HOS simulations were conducted at $k_p h = 10$ within their framework, the resulting relationship between BFI and ($\mathcal{K}_{max} - 3$) would likewise exhibit an approximately linear trend. Considering that the fully nonlinear simulations show an overshoot in kurtosis that cannot be captured by four-wave interactions, the relation between BFI and excess kurtosis at its asymptotic state (here, approximated as at $t/T_p = 200$), denoted by ($\mathcal{K}_\infty - 3$), is also presented in figure 18 to ensure the expected quadratic behaviour is adequately accounted for. A similar linear correlation is also found

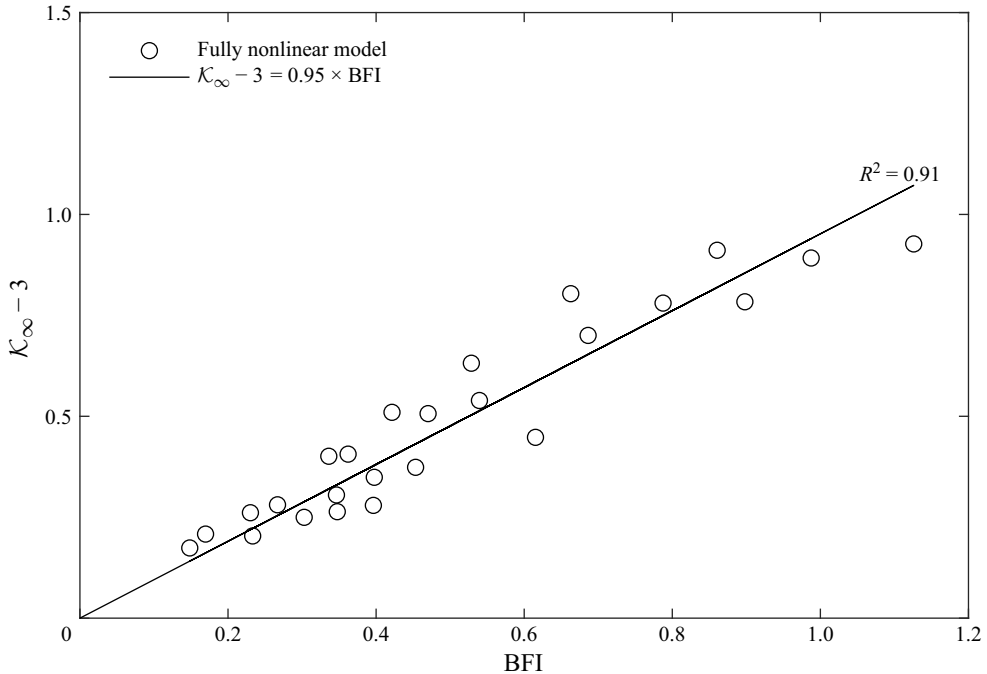$$\mathcal{K}_\infty - 3 = 0.95 \times \text{BFI}, \tag{5.7}$$

Figure 18. The relation between BFI and the excess kurtosis ($\mathcal{K}_\infty - 3$) approximated as $\mathcal{K}$ at $t/T_p = 200$. The circles denote the present fully nonlinear simulations, and the black line represents the best fit to the present (fully nonlinear model) data.

with $R^2 = 0.91$. In conjunction with the aforementioned findings, it is demonstrated that BFI is indeed a reliable indicator of high-order nonlinear effects in the wave field.

6. Conclusions

In the present work, we have presented a numerical study of the MI of wave trains and statistical properties of the surface elevation of irregular wave fields, with emphasis on the role of the dimensionless water depth $k_p h$. The study has been performed using the fully nonlinear numerical model of Klahn *et al.* (2021*d*), which is spectrally accurate in both horizontal and vertical spatial directions and maintains good computational efficiency.

We have first focused on the numerical study of wave instability phenomenon in terms of the 1-D Benjamin–Feir (class I type) instability in deep water. The initial exponential growth rates of both sidebands have been verified against analytical predictions. The simulated cases involving modulated regular wave trains have been compared with both theoretical predictions for the initial growth and experimental measurements for the longer term dynamics. The simulated results show good agreement with the experimental data, validating the present wave model for this phenomenon. Regarding the Benjamin–Feir instability, our long-time simulations illustrate both a recurrence cycle (at low initial wave steepness) and permanent frequency downshift (at higher initial wave steepness), in accordance with previous studies.

Subsequently, unidirectional irregular wave fields in finite water depths have been investigated. We have presented a detailed description of the statistical properties of the surface elevation. The skewness, the kurtosis, as well as the PDFs for both the surface elevation and wave crests, have been presented as a function of water depth. Results have

been compared with the recent work of Liu *et al.* (2022), in finite depth based on the HOS method truncated at third-order, which can only predict the statistical properties of the surface elevation related to lower-order wave–wave interactions. The present study has been able to simulate the effects of full nonlinearity on wave statistical properties. The present simulations have demonstrated higher kurtosis, a greater manifestation of MI and exhibit more pronounced non-Gaussian wave statistics than predicted by the HOS method across all water depths. As the water depth decreases, the differences between the two diminish. Hence, we conclude that third-order HOS simulations generally (significantly) under-predict the occurrence of rogue waves, at least in 1-D simulations.

We have also elucidated the importance of full nonlinearity for MI in the evolution of unidirectional wave fields at finite depth using more extensive fully nonlinear simulations. For waves in finite depth we have found that the kurtosis, and hence the occurrence probability of a rogue wave, can be predicted by the BFI. According to third-order HOS results, the maximum excess kurtosis is linearly related to the square of BFI (i.e. $(\mathcal{K}_{max} - 3) \propto \text{BFI}^2$). This is no longer the case for wave fields including fully nonlinear wave–wave interactions. Considering full nonlinearity, we have found that a new linear relationship between maximal kurtosis and BFI (i.e. $\mathcal{K}_{max} - 3 \propto \text{BFI}$), with stronger correlation than found previously based on third-order HOS results. It is noteworthy that the newly identified linear relationship appears universal over a broad range of water depths, specifically for dimensionless depth conditions having $k_p h \geqslant 1.5$.

Declaration of interests. The authors report no conflict of interest.

Data availability statement. Data utilised in the present study are freely available at https://doi.org/10.11583/DTU.27247275. The data set includes the surface elevation generated by the fully nonlinear PFL model of Klahn *et al.* (2021*d*) utilised in the present work. Additionally, a Matlab function pdf6.m returning the new PDFs of sixth order in nonlinearity is also freely provided at: https://doi.org/10.11583/DTU.24720564.

Appendix A. Determining PDFs up to sixth order based on Klahn *et al.* (2024)

Klahn *et al.* (2024) provided the coefficients required to obtain the theoretical PDF of the surface elevation up to fifth order. As PDFs up to sixth order have been presented in the present work (§ 4), we will therefore provide the required additional coefficients and other details required to obtain the PDF at this new order in the present appendix.

From (2.7) of Klahn *et al.* (2024), the ordinary differential equation governing the PDF at sixth order corresponds to

$$0 = \zeta p + \kappa_2 \frac{\mathrm{d}p}{\mathrm{d}\zeta} - \frac{\kappa_3}{2}\frac{\mathrm{d}^2 p}{\mathrm{d}\zeta^2} + \frac{\kappa_4}{6}\frac{\mathrm{d}^3 p}{\mathrm{d}\zeta^3} - \frac{\kappa_5}{24}\frac{\mathrm{d}^4 p}{\mathrm{d}\zeta^4} + \frac{\kappa_6}{120}\frac{\mathrm{d}^5 p}{\mathrm{d}\zeta^5} - \frac{\kappa_7}{720}\frac{\mathrm{d}^6 p}{\mathrm{d}\zeta^6}, \quad \text{(A1)}$$

in which κ_n is the nth cumulant of ζ. Expressions for these cumulants in terms of the statistical moments are provided in table 3. As explained by Klahn *et al.* (2024), asymptotic solutions at the $\zeta \to \infty$ limit to (A1) can be found through the method of dominant balance. Following their procedure leads to the following asymptotic solution for the positive tail of $p(\zeta)$ at sixth order:

$$p(\zeta) \sim \frac{B}{\zeta^{a_0}} \exp\left(a_1 \zeta^{7/6} + a_2 \zeta + a_3 \zeta^{5/6} + a_4 \zeta^{2/3} + a_5 \zeta^{1/2} + a_6 \zeta^{1/3} + a_7 \zeta^{1/6}\right), \quad \text{(A2)}$$

κ_1	κ_2	κ_3	κ_4	κ_5	κ_6	κ_7
0	1	$\mathcal{S}$	$\mathcal{K}-3$	$\mathcal{S}_h - 10\mathcal{S}$	$30 - 15\mathcal{K} - 10\mathcal{S}^2 + \mathcal{K}_h$	$210\mathcal{S} - 35\mathcal{K}\mathcal{S} - 21\mathcal{S}_h + m_7$

Table 3. The first seven cumulants expressed in terms of the skewness $\mathcal{S}$, kurtosis $\mathcal{K}$, hyperskewness $\mathcal{S}_h \equiv \langle \zeta^5 \rangle$, hyperkurtosis $\mathcal{K}_h \equiv \langle \zeta^6 \rangle$ and $m_7 \equiv \langle \zeta^7 \rangle$.

a_0	$-\dfrac{5}{12}$
a_1	$-\dfrac{6}{7}\left(\dfrac{720}{\kappa_7}\right)^{1/6}$
a_2	$\dfrac{\kappa_6}{\kappa_7}$
a_3	$\dfrac{3^{2/3}(2\kappa_5\kappa_7 - \kappa_6^2)}{2^{2/3} \times 5^{1/6}\kappa_7^{11/6}}$
a_4	$\dfrac{5^{2/3}(\kappa_6^3 - 3\kappa_5\kappa_6\kappa_7 + 3\kappa_4\kappa_7^2)}{3^{2/3} \times 2^{1/3}\kappa_7^{8/3}}$
a_5	$\dfrac{5^{1/2}(-9\kappa_6^4 + 36\kappa_5\kappa_6^2\kappa_7 - 20\kappa_5^2\kappa_7^2 - 32\kappa_4\kappa_6\kappa_7^2 + 32\kappa_3\kappa_7^3)}{16\kappa_7^{7/2}}$
a_6	$\dfrac{2^{1/3}(14\kappa_6^5 - 70\kappa_5\kappa_6^3\kappa_7 + 75\kappa_5^2\kappa_6\kappa_7^2 + 60\kappa_4\kappa_6^2\kappa_7^2 - 75\kappa_4\kappa_5\kappa_7^3 - 45\kappa_3\kappa_6\kappa_7^3 + 45\kappa_7^4)}{3 \times 3^{1/3} \times 5^{2/3}\kappa_7^{13/3}}$
a_7	$\dfrac{5^{1/6}(1729\kappa_6^6 - 10\,374\kappa_5\kappa_6^4\kappa_7 + 16\,380\kappa_5^2\kappa_6^2\kappa_7^2 + 8736\kappa_4\kappa_6^3\kappa_7^2 - 4200\kappa_5^3\kappa_7^3 - 20\,160\kappa_4\kappa_5\kappa_6\kappa_7^3 - 6048\kappa_3\kappa_6^2\kappa_7^3 + 5760\kappa_4^2\kappa_7^4 + 8640\kappa_3\kappa_5\kappa_7^4 + 3456\kappa_6\kappa_7^4)}{-576 \times 2^{1/3} \times 3^{2/3}\kappa_7^{31/6}}$

Table 4. The coefficients in the asymptotic form of $p(\zeta)$ (see (A2)) at sixth order.

where the coefficients $a_0, a_1, \ldots, a_7$ are listed in table 4. Utilising an assumed value of B, boundary conditions for $p(\zeta)$ and its first six derivatives at $\zeta = \zeta_{max}$ can be established from (A2). Utilising these, (A1) may then be numerically integrated backwards from ζ_{max} to the first zero crossing at ζ_{min}. As discussed by Klahn *et al.* (2024), the solution turns oscillatory for $\zeta < \zeta_{min}$, and hence this part of the solution may be discarded. All results in the present study have utilised $\zeta_{max} = 9$. The correct value of B is then found iteratively, such that

$$\int_{\zeta_{min}}^{\zeta_{max}} p(\zeta)\mathrm{d}\zeta = 1, \tag{A3}$$

leading to the sixth-order PDFs presented in the present work. Functions automating this procedure up to sixth order are provided at the URL indicated in the data availability statement.

REFERENCES

ADCOCK, T.A.A. & TAYLOR, P.H. 2014 The physics of anomalous ('rogue') ocean waves. *Rep. Prog. Phys.* **77** (10), 105901.

ANNENKOV, S.Y. & SHRIRA, V.I. 2009 Evolution of kurtosis for wind waves. *Geophys. Res. Lett.* **36** (13), L13603.

BABANIN, A.V., HSU, T.-W., ROLAND, A., OU, S.-H., DOONG, D.-J. & KAO, C.C. 2011 Spectral wave modelling of typhoon Krosa. *Nat. Hazards Earth Syst. Sci.* **11** (2), 501–511.

BANNER, M.L. & TIAN, X. 1998 On the determination of the onset of breaking for modulating surface gravity waves. *J. Fluid Mech.* **367**, 107–137.

BENJAMIN, T.B. & FEIR, J.E. 1967 The disintegration of wave trains on deep water. Part 1. Theory. *J. Fluid Mech.* **27** (3), 417–430.

BOUWS, E., GÜNTHER, H., ROSENTHAL, W. & VINCENT, C.L. 1985 Similarity of the wind wave spectrum in finite depth water: 1. Spectral form. *J. Geophys. Res. Oceans* **90** (C1), 975–986.

CHALIKOV, D. 2009 Freak waves: their occurrence and probability. *Phys. Fluids* **21** (7), 076602.

CHIEN, H.W.A., KAO, C.-C. & CHUANG, L.Z.H. 2002 On the characteristics of observed coastal freak waves. *Coast. Engng J.* **44** (04), 301–319.

DAVEY, A. & STEWARTSON, K. 1974 On three-dimensional packets of surface waves. *Proc. R. Soc. Lond. A.* **338**, 101–110, 1613.

DOMMERMUTH, D.G. & YUE, D.K.P. 1987 A high-order spectral method for the study of nonlinear gravity waves. *J. Fluid Mech.* **184**, 267–288.

DONG, G., LIAO, B., MA, Y. & PERLIN, M. 2018 Experimental investigation of the peregrine breather of gravity waves on finite water depth. *Phys. Rev. Fluids.* **3** (6), 064801.

DYSTHE, K., KROGSTAD, H.E. & MÜLLER, P. 2008 Oceanic rogue waves. *Annu. Rev. Fluid Mech.* **40**, 287–310.

DYSTHE, K.B., TRULSEN, K., KROGSTAD, H.E. & SOCQUET-JUGLARD, H. 2003 Evolution of a narrow-band spectrum of random surface gravity waves. *J. Fluid Mech.* **478**, 1–10.

FEDELE, F., HERTERICH, J., TAYFUN, M.A. & DIAS, F. 2019 Large nearshore storm waves off the Irish coast. *Sci. Rep.* **9** (1), 15406.

FEDELE, F. & TAYFUN, M.A. 2009 On nonlinear wave groups and crest statistics. *J. Fluid Mech.* **620**, 221–239.

FENTON, J.D. 1988 The numerical solution of steady water wave problems. *Comput. Geosci.* **14** (3), 357–368.

FERNANDEZ, L., ONORATO, M., MONBALIU, J. & TOFFOLI, A. 2014 Modulational instability and wave amplification in finite water depth. *Nat. Hazards Earth Syst. Sci.* **14** (3), 705–711.

FORRISTALL, G.Z. 2005 Understanding rogue waves: are new physics really necessary?. In *Rogue Waves: Proc. 14th 'Aha Huliko'a Hawaiian Winter Workshop*, pp. 29–35. University of Hawaii.

FUHRMAN, D.R. & BINGHAM, H.B. 2004 Numerical solutions of fully non-linear and highly dispersive Boussinesq equations in two horizontal dimensions. *Intl J. Numer. Meth. Fluids* **44**, 231–255.

FUHRMAN, D.R., KLAHN, M. & ZHAI, Y. 2023 A new probability density function for the surface elevation in irregular seas. *J. Fluid Mech.* **970**, A38.

FUHRMAN, D.R., MADSEN, P.A. & BINGHAM, H. 2004 A numerical study of crescent waves. *J. Fluid Mech.* **513**, 309–341.

GRAMSTAD, O. & TRULSEN, K. 2011 Hamiltonian form of the modified nonlinear Schrödinger equation for gravity waves on arbitrary depth. *J. Fluid Mech.* **670**, 404–426.

HAYER, S. & ANDERSEN, O.J. 2000 Freak waves: rare realizations of a typical population or typical realizations of a rare population? In *Proc. 10th ISOPE. Conf*, pp. ISOPE–I–00-233. International Society Offshore & Polar Engineers.

HENDERSON, K.L., PEREGRINE, D.H. & DOLD, J.W. 1999 Unsteady water wave modulations: fully nonlinear solutions and comparison with the nonlinear schrödinger equation. *Wave Motion* **29** (4), 341–361.

HOLTHUIJSEN, L.H. 2010 *Waves in Oceanic and Coastal Waters*. Cambridge University Press.

JANSSEN, P.A.E.M. 2003 Nonlinear four-wave interactions and freak waves. *J. Phys. Oceanogr.* **33** (4), 863–884.

JANSSEN, P.A.E.M. & BIDLOT, J.-R. 2009 *On the Extension of the Freak Wave Warning System and its Verification (Technical Memorandum)*. ECMWF.

JANSSEN, P.A.E.M. & ONORATO, M. 2007 The intermediate water depth limit of the Zakharov equation and consequences for wave prediction. *J.Phys. Oceanogr.* **37** (10), 2389–2400.

KARMPADAKIS, I., SWAN, C. & CHRISTOU, M. 2019 Laboratory investigation of crest height statistics in intermediate water depths. *Proc. R. Soc. Lond. A* **475**, 20190183.

KHARIF, C. & PELINOVSKY, E. 2003 Physical mechanisms of the rogue wave phenomenon. *Eur. J. Mech. B Fluids* **22** (6), 603–634.

KHARIF, C., PELINOVSKY, E. & SLUNYAEV, A. 2008 *Rogue Waves in the Ocean*. Springer Science & Business Media.

KLAHN, M., MADSEN, P.A. & FUHRMAN, D.R. 2021*a* Mean and variance of the Eulerian and Lagrangian horizontal velocities induced by nonlinear multi-directional irregular water waves. *Proc. R. Soc. Lond. A.* **477**, 20210516.

KLAHN, M., MADSEN, P.A. & FUHRMAN, D.R. 2021*b* On the statistical properties of inertia and drag forces in nonlinear multi-directional irregular water waves. *J. Fluid Mech.* **916**, A59.

KLAHN, M., MADSEN, P.A. & FUHRMAN, D.R. 2021*c* On the statistical properties of surface elevation, velocities and accelerations in multi-directional irregular water waves. *J. Fluid Mech.* **910**, A23.

KLAHN, M., MADSEN, P.A. & FUHRMAN, D.R. 2021*d* Simulation of three-dimensional nonlinear water waves using a pseudospectral volumetric method with an artificial boundary condition. *Intl J. Numer. Meth. Fluids* **93** (6), 1843–1870.

KLAHN, M., ZHAI, Y. & FUHRMAN, D.R. 2024 Heavy tails and probability density functions to any nonlinear order for the surface elevation in irregular seas. *J. Fluid Mech.* **985**, A35.

LANDRINI, M., OSHRI, O., WASEDA, T. & TULIN, M.P. 1998 Long time evolution of gravity wave systems. In *Proc. 13th Intl Workshop on Water Waves and Floating Bodies (ed. AJ Hermans), Alphen aan den Rijn*, pp. 75–78. Delft University of Technology.

LAVRENOV, I.V. 1998 The wave energy concentration at the Agulhas current off South Africa. *Nat. Hazards* **17**, 117–127.

LI, Y. & FUHRMAN, D.R. 2022 Computational fluid dynamics simulation of deep-water wave instabilities involving wave breaking. *J. Offshore Mech. Arct. Engng* **144** (2), 021901.

LIU, S., ZHANG, X., YANG, J. & YAO, J. 2022 Modulational instability and statistical properties of irregular waves in finite water depth. *Appl. Ocean Res.* **120**, 103031.

LO, E. & MEI, C.C. 1985 A numerical study of water-wave modulation based on a higher-order nonlinear Schrödinger equation. *J. Fluid Mech.* **150**, 395–416.

MADSEN, P.A., BINGHAM, H.B. & LIU, H. 2002 A new Boussinesq method for fully nonlinear waves from shallow to deep water. *J. Fluid Mech.* **462**, 1–30.

MCLEAN, J.W. 1982*a* Instabilities of finite-amplitude gravity waves on water of finite depth. *J. Fluid Mech.* **114**, 331–341.

MCLEAN, J.W. 1982*b* Instabilities of finite-amplitude water waves. *J. Fluid Mech.* **114**, 315–330.

MELVILLE, W.K. 1982 The instability and breaking of deep-water waves. *J. Fluid Mech.* **115**, 165–185.

MORI, N. & JANSSEN, P.A.E.M. 2006 On Kurtosis and occurrence probability of freak waves. *J. Phys. Oceanogr.* **36** (7), 1471–1483.

MORI, N. & YASUDA, T. 2002 A weakly non-Gaussian model of wave height distribution for random wave train. *Ocean Engng* **29** (10), 1219–1231.

NICHOLLS, D.P. 2011 Efficient enforcement of far-field boundary conditions in the transformed field expansions method. *J. Comput. Phys.* **230** (22), 8290–8303.

ONORATO, M. 2009 Statistical properties of mechanically generated surface gravity waves: a laboratory experiment in a three-dimensional wave basin. *J. Fluid Mech.* **627**, 235–257.

ONORATO, M., OSBORNE, A.R., SERIO, M. & BERTONE, S. 2001 Freak waves in random oceanic sea states. *Phys. Rev. Lett.* **86** (25), 5831.

ONORATO, M., OSBORNE, A.R., SERIO, M., CAVALERI, L., BRANDINI, C. & STANSBERG, C.T. 2004 Observation of strongly non-Gaussian statistics for random sea surface gravity waves in wave flume experiments. *Phys. Rev. E* **70** (6), 067302.

ONORATO, M., OSBORNE, A.R., SERIO, M., CAVALERI, L., BRANDINI, C. & STANSBERG, C.T. 2006 Extreme waves, modulational instability and second order theory: wave flume experiments on irregular waves. *Eur. J. Mech. B Fluids* **25** (5), 586–601.

ONORATO, M., OSBORNE, A.R., SERIO, M., RESIO, D., PUSHKAREV, A., ZAKHAROV, V.E. & BRANDINI, C. 2002 Freely decaying weak turbulence for sea surface gravity waves. *Phys. Rev. Lett.* **89** (14), 144501.

ONORATO, M., PROMENT, D., EL, G., RANDOUX, S. & SURET, P. 2016 On the origin of heavy-tail statistics in equations of the nonlinear Schrödinger type. *Phys. Lett. A* **380** (39), 3173–3177.

ONORATO, M., RESIDORI, S., BORTOLOZZO, U., MONTINA, A. & ARECCHI, F.T. 2013 Rogue waves and their generating mechanisms in different physical contexts. *Phys. Rep.* **528** (2), 47–89.

SHEMER, L. & SERGEEVA, A. 2009 An experimental study of spatial evolution of statistical parameters in a unidirectional narrow-banded random wavefield. *J. Geophys. Res.* **114** (C1), C01015.

SHEMER, L., SERGEEVA, A. & SLUNYAEV, A. 2010 Applicability of envelope model equations for simulation of narrow-spectrum unidirectional random wave field evolution: experimental validation. *Phys. Fluids.* **22** (1), 016601.

SLUNYAEV, A., DIDENKULOVA, I. & PELINOVSKY, E. 2011 Rogue waters. *Contemp. Phys.* **52** (6), 571–590.

SLUNYAEV, A.V. & SERGEEVA, A.V. 2012 Stochastic simulation of unidirectional intense waves in deep water applied to rogue waves. *JETP Lett.* **94**, 779–786.

TAYFUN, M.A. 1980 Narrow-band nonlinear sea waves. *J. Geophys. Res.* **85**, 1548–1552.

TAYFUN, M.A. & ALKHALIDI, M.A. 2020 Distribution of sea-surface elevations in intermediate and shallow water depths. *Coast. Engng* **157**, 103651.

TAYFUN, M.A. & FEDELE, F. 2007 Wave-height distributions and nonlinear effects. *Ocean Engng* **34** (11–12), 1631–1649.

TOFFOLI, A., GRAMSTAD, O., TRULSEN, K., MONBALIU, J., BITNER-GREGERSEN, E. & ONORATO, M. 2010 Evolution of weakly nonlinear random directional waves: laboratory experiments and numerical simulations. *J. Fluid Mech.* **664**, 313–336.

TOFFOLI, A., ONORATO, M., BABANIN, A.V., BITNER-GREGERSEN, E., OSBORNE, A.R. & MONBALIU, J. 2007 Second-order theory and setup in surface gravity waves: a comparison with experimental data. *J. Phys. Oceanogr.* **37** (11), 2726–2739.

TRULSEN, K. 2007 Weakly nonlinear sea surface waves – freak waves and deterministic forecasting. In *Geometric Modelling, Numerical Simulation, and Optimization: Applied Mathematics at SINTEF*, pp. 191–209. Springer Berlin Heidelberg.

TULIN, M.P. & WASEDA, T. 1999 Laboratory observations of wave group evolution, including breaking effects. *J. Fluid Mech.* **378**, 197–232.

WEST, B.J., BRUECKNER, K.A., JANDA, R.S., MILDER, D.M. & MILTON, R.L. 1987 A new numerical method for surface hydrodynamics. *J. Geophys. Res. Oceans* **92** (C11), 11803–11824.

WHITE, B.S. & FORNBERG, B. 1998 On the chance of freak waves at sea. *J. Fluid Mech.* **355**, 113–138.

WHITHAM, G.B. 1974 Linear and Nonlinear Waves. John Wiley & Sons.

XIAO, W. 2013 Study of directional ocean wavefield evolution and rogue wave occurrence using large-scale phase-resolved nonlinear simulations *PhD thesis*, Massachusetts Institute of Technology, USA.

XIAO, W., LIU, Y., WU, G. & YUE, D.K.P. 2013 Rogue wave occurrence and dynamics by direct simulations of nonlinear wave-field evolution. *J. Fluid Mech.* **720**, 357–392.

ZAKHAROV, V.E. 1968 Stability of periodic waves of finite amplitude on the surface of a deep fluid. *J. Appl. Mech. Tech. Phys.* **9** (2), 190–194.

ZAKHAROV, V.E., DYACHENKO, A.I. & VASILYEV, O.A. 2002 New method for numerical simulation of a nonstationary potential flow of incompressible fluid with a free surface. *Eur. J. Mech. B Fluids* **21** (3), 283–291.